Algebraic flux correction finite element method with semi-implicit time stepping for solute transport in fractured porous media

Konstantin Brenner, Nejmeddine Chorfi, Roland Masson

Algebraic flux correction finite element method with semi-implicit time stepping for solute transport in fractured porous media

Konstantin Brenner[1,2], Nejmeddine Chorfi[3], and Roland Masson[1,2]

[1]Team COFFEE, Inria Sophia-Antipolis - Méditerranée, Valbonne, France
[2]Université Côte d'Azur, CNRS, Laboratoire J.A. Dieudonné, Nice, France
[3]King Saud University, Riyadh, Saudi Arabia

Abstract

This work is concerned with the numerical modeling of the Darcy flow and solute transport in fractured porous media for which the fractures are modeled as interfaces of codimension one. The hybrid-dimensional flow and transport problems are discretizaed by a lumped piecewise linear finite element method, combined with the algebraic correction of the convective fluxes. The resulting transport discretization can be interpreted as a conservative finite volume scheme that satisfies the discrete maximum principle, while introducing a very limited amount of numerical diffusion.

In the context of fractured porous media flow the CFL number may vary by several order of magnitude, which makes explicit time stepping unfeasible. To cope with this difficulty we propose an adaptive semi-implicit time stepping strategy that reduces to the low order linear implicit discretization in the high CFL regions that include, but may not be limited to the fracture network. The performance of the fully explicit and semi-implicit variants of the method are investigated through the numerical experiment.

Keywords: Discrete matrix fracture model, transport equation, finite element method, finite volume method, algebraic flux correction.

1 Introduction

Flow and transport in fractured porous media are key processes in many subsurface applications such as geothermal energy production, CO2 sequestration, or geological waste storage. In this article, we consider a so-called hybrid-dimensional or Discrete Fracture Matrix (DFM) model, where the fractures are geometrically represented as surfaces of codimension one embedded into the surrounding porous matrix. The reduced flow and transport equations are obtained by averaging the physical unknowns as well as the conservation equations across the fracture width, and by imposing some appropriate transmission conditions at the matrix fracture interfaces [2], [32]. Compared to the equi-dimensional representation of the fracture network, the hybrid-dimensional approach facilitates the mesh generation and is likely to reduce the computational cost of the resulting numerical scheme [10]. Due to the ubiquity of fractures in geology and their considerable impact on the flow and transport in the porous medium the DFM models have been intensively studied over the last two decades. We refer to [9] and [6] for review of the relevant literature.

The tetrahedral (triangular in 2d) meshes are commonly used to cope with the geometrical complexity of fracture networks. In this context, nodal discretizations have a clear advantage over cell-centered or face based ones, since they lead to a much lower number of degrees of freedom (dofs). Those nodal methods usually combine the discretization techniques from Finite Element (FE) and Finite Volume (FV) methods. In particular they rely on the FE

Corresponding author: Konstantin Brenner, Université Côte d'Azur, CNRS, Inria, LJAD, Parc Valrose, 06108, Nice, France, konstantin.brenner@univ-cotedazur.fr

representation of the pressure, while the main ingredients borrowed from the FV framework is the lumping of the mass matrix and the stable discretization of the transport terms.

The nodal FV-FE are locally conservative with respect to some nodal control volumes. This is achieved by constructing the conservative edge fluxes that account for the mass exchange between the neighboring nodes. In addition the use of the FV techniques allows to design the numerical schemes that are *monotone* in the sense that the maximum principle is preserved at the discrete level. In order to insure the latter property the convection term has to be treated either by the first order linear upwinding scheme or by a nonlinear higher-order method. The nodal DFM discretizations using the linear upwinding can be found in [34], [36], [35], [39], [38], [7], [8] and [10]. Those first order schemes lead in general to overly diffused solutions. The numerical diffusion can be reduced by combining the higher-order flux approximation with some nonlinear flux limiting procedure [45], [41], [44]. Nodal FV-FE schemes of this kind have been proposed in [14] and [42] for multi-phase DFM flow, and in [33] for DFM passive transport problem. Alternatively, the monotone higher-order methods for DFM flow and transport have been designed in [46], [47], [22] using cell-centered FV approach, in [16], [17], [19], [18], [50] using Mixed FE method coupled to Discontinuous Galerkin discretization, and in [15], [23] in the context of the embedded DFM methodology.

The alternative to the geometrical slope limiting [49] is the Algebraic Flux Correction approach, which has been actively developed over the past two decades . Roughly speaking the AFC framework provides the road map on how to transform a high-order discretization (typically a Galerkin FE method) into a monotone nonlinear scheme. This is achieved by combining the high-order baseline discretization with a low order monotone method, which provides a required amount of numerical diffusion. Compared to the traditional geometric slope limiting [49], the AFC methods only rely on the topology of the mesh and the matrix coefficients resulting from the baseline discretization, and therefore, can be easily implemented within existing finite element codes. The AFC method was originally introduced in [24] and [28] for the multi-dimentional linear transport problem, and then further extended to the hyperbolic systems [26] and elliptic problems [27], [3]. Let us particularly mention [37] where the AFC method has been applied to flow and transport in fractured porous media in the context of equi-dimensional fracture network representation. A recent review of the AFC methods can be found in [4] and [30].

In this work we apply the FE-AFC method from [26] in the context of DFM flow and transport. We consider the single-phase Darcy flow problem under continuous pressure assumption combined with a passive tracer transport in matrix and fracture domains. We use the piecewise linear FE method both to discretize the flow problem and as the baseline method of the AFC discretization of the transport equation. We show that the resulting transport scheme can be interpreted as a conservative nodal FV-FE method. We note that in contrast to the existing high-order nodal FE-FV schemes, such as in [14], [33] or [42], our method does not require the construction of any dual grid.

As it has been pointed out in [18] and [33] the numerical DFM flow models are characterized by the CFL number that may vary by several orders of magnitude. This is essentially due to the high permeability contrast between the fracture and the matrix domains. In addition, the geometrical complexity of the realistic fracture networks is likely to result in the locally refined meshes, which, again, contributes to the variability of the CFL number. In this context, the use of the time stepping methods based on the global CFL constraint may not be practical. Following [18] and [33] we propose the semi-implicit time discretization that treats low and high CFL regions differently. In the regions where the local CFL constraint is acceptable we use the nonlinear explicit AFC method, while the high CFL zones are treated with the lower order linear implicit scheme. In practice, the CFL constraint can be significantly relaxed if the implicit time stepping zone is identified with the fracture network. Our numerical experiment shows that the low-order implicit discretization of the fracture domain is sufficient to capture accurately the concentration profiles at the large time scale. In addition, we show that extending the implicit zone to a small portion of the matrix mesh elements allows to further increase the stable time step by the few orders of magnitude without affecting the overall accuracy.

2 Continuous problem

Let Ω be an open bounded domain of $\mathbb{R}^d$, $d = 2, 3$, assumed to be polyhedral for $d = 3$ (and polygonal for $d = 2$). To fix ideas the dimension will be fixed to $d = 3$ when it needs to be specified, for instance in the naming of the geometrical objects or for the space discretization in the next section. The adaptations to the case $d = 2$ are straightforward. Let $\overline{\Gamma} = \bigcup_{k\in\mathcal{I}} \overline{\Gamma}_k$

denotes the network of fractures $\Gamma_k \subset \Omega, k \in \mathcal{I}$, such that each Γ_k is a planar polygonal simply connected open domain included in some plane of $\mathbb{R}^d$. Without restriction of generality, we will assume that the fractures may intersect exclusively at their boundaries (see Figure 1), that is for any $k, l \in \mathcal{I}, k \neq l$ one has $\Gamma_k \cap \Gamma_l = \emptyset$, but not necessarily $\overline{\Gamma}_k \cap \overline{\Gamma}_l = \emptyset$.

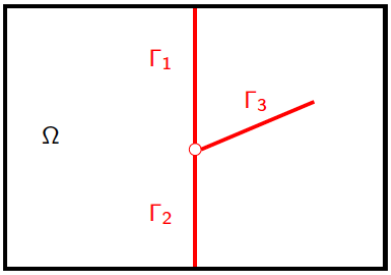

Figure 1: Example of a 2D domain Ω with 3 intersecting fractures $\Gamma_k, k = 1, 2, 3$.

In the matrix domain, defined as $\Omega_m = \Omega \setminus \overline{\Gamma}$, (resp. in the fracture network Γ), we denote by $\phi_m(\mathbf{x})$ (resp. $\phi_f(\mathbf{x})$) the porosity and by $\Lambda_m(\mathbf{x})$ (resp. $\Lambda_f(\mathbf{x})$) the permeability (resp. tangential permeability) tensor. The thickness of the fractures is denoted by $d_f(\mathbf{x})$ for $\mathbf{x} \in \Gamma$. Let p_m and p_f denote the pressure fields defined over Ω_m and Γ respectively, neglecting the gravity we define the corresponding Darcy velocity fields $\mathbf{q}_m$ and $\mathbf{q}_f$ as

$$\mathbf{q}_m = -\Lambda_m \nabla p_m \qquad \text{and} \qquad \mathbf{q}_f = -d_f \Lambda_f \nabla_\tau p_f,$$

where ∇_τ is the $d-1$ dimensional gradient operator tangential to Γ. Because of the mass exchange occurring at the matrix-fracture interface the normal trace of $\mathbf{q}_m$ is in general discontinuous across Γ. The jump of the normal trace of $\mathbf{q}_m$ will be denoted by $[\![\mathbf{q}_m \cdot \mathbf{n}]\!]_\Gamma$. Let div_τ denote the $d-1$ tangential to Γ divergence operator. Assuming the incompressible flow, the mixed-dimensional volume conservation law is expressed as

$$\mathrm{div}\mathbf{q}_m = 0 \quad \text{in} \quad \Omega_m \tag{1}$$

and

$$\mathrm{div}_\tau \mathbf{q}_f = [\![\mathbf{q}_m \cdot \mathbf{n}]\!]_\Gamma \quad \text{in} \quad \Gamma. \tag{2}$$

We suppose that the pressure fields p_m and p_f satisfy some Dirichlet boundary conditions imposed on $\partial\Omega_D \subset \partial\Omega$ and $\partial\Gamma_D := \partial\Omega_D \cap \partial\Gamma$ respectively, while the remainder of the boundary is subject to the no-flow condition

$$\begin{array}{lll} \mathbf{q}_m \cdot \mathbf{n} = 0 & \text{on} & \partial\Omega \setminus \partial\Omega_D, \\ \mathbf{q}_f \cdot \mathbf{n} = 0 & \text{on} & \partial\Gamma \setminus \partial\Omega_D. \end{array} \tag{3}$$

Note that (3) also implies the classical no-flux condition at the tips of the fractures.

To close the system (1)-(3) we have to prescribe some transmission condition at the matrix-fracture interface. In this article we assume the so-called continuous pressure model introduced in [2]. More specifically p_m is assumed to be continuous across Γ, while the fracture pressure p_f coincides with the trace of p_m on Γ. In a single phase flow setting those assumptions are relevant for the fractures acting as drains. For the discussion on more general transmission condition and the model comparison we refer to [12], [32], [10], [1], [13] and [5].

Let c_m and c_f denote the tracer concentration fields defined over Ω_m and Γ respectively. The tracer volume conservation in the matrix and the fracture domains reads as

$$\phi_m \partial_t c_m + \mathrm{div}(c_m \mathbf{q}_m) = 0 \quad \text{in} \quad \Omega_m \tag{4}$$

and

$$d_f \phi_f \partial_t c_f + \mathrm{div}_\tau(c_f \mathbf{q}_f) \quad = \quad [\![c_m \mathbf{q}_m \cdot \mathbf{n}]\!]_\Gamma \quad \text{in} \quad \Gamma. \tag{5}$$

The system (4)-(5) system should be complemented by some initial conditions, as well as some Dirichlet condition imposed on the inflow part of the boundary

$$\partial\Omega_D^- = \{\mathbf{x} \in \partial\Omega_D | \, \mathbf{q}_m \cdot \mathbf{n} < 0\} \qquad \text{and} \qquad \partial\Gamma_D^- = \{\mathbf{x} \in \partial\Gamma_D | \, \mathbf{q}_f \cdot \mathbf{n} < 0\}.$$

More over, as in the case of the pressure problem, we have to prescribe a closure condition on matrix-fracture interface. Since we are dealing here with the hyperbolic equations, we can

not, in general, expect the solution to be continuous across the fracture. In order to avoid the unnecessary technicality the matrix-fracture transmission condition will not be specified for the continuous model. Roughly speaking, it states of the continuity of the fracture and the matrix concentration fields at the inflow boundary of the matrix domain $\Omega_m = \Omega \setminus \Gamma$, for more details we refer to [48], we also refer to [11] for some specific energy stable transition condition for advection-diffusion DFM problems. At the discrete level we will be imposing the continuity of tracer concentration at the matrix-fracture interface, which is the common practice for the nodal FV-FE methods (see e.g. [34], [19], [18], [38], [33], [7] and [9]).

Let $\psi \in C^\infty(\Omega)$, multiplying (1) and (2) by ψ, performing the integration by parts, and adding the contributions of the matrix and fracture domains we obtain

$$\int_{\Omega_m} \nabla\psi \cdot \mathbf{q}_m \,\mathrm{d}\mathbf{x} + \int_\Gamma \nabla_\tau\psi \cdot \mathbf{q}_f \,\mathrm{d}\sigma(\mathbf{x}) - \int_{\partial\Omega_D} \psi\, \mathbf{q}_m \cdot \mathbf{n} \,\mathrm{d}\sigma(\mathbf{x}) - \int_{\partial\Gamma_D} \psi\, \mathbf{q}_f \cdot \mathbf{n} \,\mathrm{d}l(\mathbf{x}) = 0 \quad (6)$$

in view of (3). Similarly (4) and (5) lead to

$$\begin{aligned} \int_{\Omega_m} \psi\phi_m \partial_t c_m \,\mathrm{d}\mathbf{x} + \int_\Gamma \psi d_f \phi_f \partial_t c_f \,\mathrm{d}\sigma(\mathbf{x}) &= \int_{\Omega_m} c_m \nabla\psi \cdot \mathbf{q}_m \,\mathrm{d}\mathbf{x} + \int_\Gamma c_f \nabla_\tau\psi \cdot \mathbf{q}_f \,\mathrm{d}\sigma(\mathbf{x}) \\ &- \int_{\partial\Omega_D} c_m \psi\, \mathbf{q}_m \cdot \mathbf{n} \,\mathrm{d}\sigma(\mathbf{x}) - \int_{\partial\Gamma_D} c_f \psi\, \mathbf{q}_f \cdot \mathbf{n} \,\mathrm{d}l(\mathbf{x}). \end{aligned} \quad (7)$$

3 Discrete problem

3.1 Space discretization

We now introduce a conforming simplical mesh. We denote by $\mathcal{T}$ a finite set of open tetrahedra (triangles if $d = 2$) such that $\cup_{T\in\mathcal{T}} \overline{T} = \overline{\Omega}$ and such that $T \cap T' = \emptyset$ for any $T \neq T'$; moreover we assume that for any $T \neq T'$ the set $\overline{T} \cap \overline{T'}$ coincides with some face, edge or a node of T and T'. The set of mesh nodes is denoted by $(\mathbf{x}_i)_{i\in\mathcal{N}}$, where $\mathcal{N} = \{1, 2, \ldots, N_{\mathrm{dof}}\}$ is the set of node indices. We denote by $\mathcal{F}$ the set of mesh faces, that are open $d-1$ simplices (triangles for $d = 3$ and segments for $d = 2$).

We assume that the mesh is conforming with respect to the geometry of the fracture network, meaning that each individual fracture Γ_k can be represented as a union of mesh faces. This can be insured by the following conditions: $T \cap \Gamma = \emptyset$ for any $T \in \mathcal{T}$ and $\sigma \cap \partial\Gamma_k = \emptyset$ for all $\sigma \in \mathcal{F}$ and $k \in \mathcal{I}$. We further assume that Λ_m and ϕ_m are constant on each $T \in \mathcal{T}$, and that Λ_f, ϕ_f and d_f are constant on each $\sigma \in \mathcal{F}_\Gamma$.

The subsets of faces and nodes associated with the fracture network are defined as $\mathcal{F}_\Gamma = \{\sigma \in \mathcal{F} |\, \sigma \cap \Gamma \neq \emptyset\}$ and $\mathcal{N}_\Gamma = \{i \in \mathcal{N} |\, \mathbf{x}_i \in \overline{\Gamma}\}$. In addition, for any element T we denote by $\mathcal{N}_T$ the set of its nodes, $\mathcal{N}_T = \{i \in \mathcal{N} |\, \mathbf{x}_i \in \overline{T}\}$. Similarly, for any face σ we denote by $\mathcal{N}_\sigma$ the set of its nodes, $\mathcal{N}_\sigma = \{i \in \mathcal{N} |\, \mathbf{x}_i \in \overline{\sigma}\}$. For all $i \in \mathcal{N}$ we further denote by $\mathcal{T}_i$ the subset of mesh elements connected to the node i, that is $\mathcal{T}_i = \{T \in \mathcal{T} |\, \mathbf{x}_i \in \overline{T}\}$, and by $\mathcal{F}_i$ the subset of mesh faces connected to the node i, that is $\mathcal{F}_i = \{\sigma \in \mathcal{F} |\, \mathbf{x}_i \in \overline{\sigma}\}$. Finally, we denote by $\mathcal{N}_i$ the set of neighboring nodes of i, that is $\mathcal{N}_i = \bigcup_{T\in\mathcal{T}_i} \mathcal{N}_T$.

We denote by V_h the standard conforming $\mathbb{P}_1$ finite element space associated with $\mathcal{T}$. Let $\mathcal{N}_D$ denote the set of Dirichlet nodes, $\{i \in \mathcal{N} |\, \mathbf{x}_i \in \overline{\partial\Omega_D}\}$, we define

$$V_{h,0} = \{v \in V_h |\, v(\mathbf{x}_i) = 0, i \in \mathcal{N}_D\}.$$

For $p_h \in V_h$ the approximate matrix (resp. fracture) pressure fields are defined as

$$p_{m,h} = p_h|_{\Omega_m} \qquad \text{and} \qquad p_{f,h} = p_h|_\Gamma.$$

Similarly the matrix and fracture concentration fields are build from a globally continuous approximation $c_h \in V_h$ as

$$c_{m,h} = c_h|_{\Omega_m} \qquad \text{and} \qquad c_{f,h} = c_h|_\Gamma.$$

3.2 FE discretization

The discrete Darcy velocities $\mathbf{q}_{m,h}$ and $\mathbf{q}_{f,h}$ are element-wise constant and are defined as

$$\mathbf{q}_{m,h}|_T = -\left(\Lambda_m \nabla p_h\right)|_T \qquad \forall T \in \mathcal{T} \qquad \text{and} \qquad \mathbf{q}_{f,h}|_\sigma = -\left(d_f \Lambda_f \nabla_\tau p_h\right)|_\sigma \qquad \forall \sigma \in \mathcal{F}_\Gamma. \quad (8)$$

The discrete pressure problem is obtained from (6) by using the test function from $V_{h,0}$ and by replacing $\mathbf{q}_m$ and $\mathbf{q}_f$ by their discrete counterparts.

Let $p_{D,h}$ be some function from V_h that approximate the Dirichlet data on $\partial\Omega_D$, the discrete pressure problem reads as: Find p_h such that $p_h - p_{D,h} \in V_{h,0}$ and such that

$$\int_{\Omega_m} \nabla\psi_h \cdot \mathbf{q}_{m,h}\,\mathrm{d}\mathbf{x} + \int_{\Gamma} \nabla_\tau\psi_h \cdot \mathbf{q}_{f,h}\,\mathrm{d}\sigma(\mathbf{x}) = 0 \quad \forall\psi_h \in V_{h,0}. \tag{9}$$

Let us now turn to the discretization of the transport problem. We begin with the baseline FE discretization in space. Let T_f be some final simulation time and let us denote by $c_h(t)$ the function that maps from $[0, T_f]$ to V_h. The FE discretization of the transport problem reads as follows

$$\begin{aligned}\int_{\Omega_m} \psi_h \partial_t c_h\,\mathrm{d}\mathbf{x} \quad &+ \quad \int_{\Gamma} \psi_h \partial_t c_h\,\mathrm{d}\sigma(\mathbf{x}) = \int_{\Omega_m} c_h \nabla\psi_h \cdot \mathbf{q}_{m,h}\,\mathrm{d}\mathbf{x} + \int_{\Gamma} c_h \nabla_\tau\psi_h \cdot \mathbf{q}_{f,h}\,\mathrm{d}\sigma(\mathbf{x}) \\ &- \quad \int_{\partial\Omega_D} c_h\psi_h\,\mathbf{q}_{m,h}\cdot\mathbf{n}\,\mathrm{d}\sigma(\mathbf{x}) - \int_{\partial\Gamma_D} c_h\psi_h\,\mathbf{q}_{f,h}\cdot\mathbf{n}\,\mathrm{d}l(\mathbf{x}) \qquad \forall\psi_h \in V_h\end{aligned} \tag{10}$$

together with some initial conditions $c_h(0) = c_{h,ini} \in V_h$ and the boundary conditions which will be specified later. Roughly speaking the concentration values are imposed at the inflow subset of $\mathcal{N}_D$.

Setting $c_h(t) = \sum_j c_j(t)\eta_j$ and using $\psi_h = \eta_i$ as the test function in (10) for all $i \in \mathcal{N}$ we obtain the following a system of ODEs

$$\widetilde{M}\frac{\mathrm{d}c}{\mathrm{d}t} = \widetilde{K}c - \left(\widetilde{S}^{+}c + \widetilde{S}^{-}c_D\right). \tag{11}$$

Here $\widetilde{M}$ is the mass matrix, $\widetilde{K} = \widetilde{K}_m + \widetilde{K}_f$ is the discrete transport operator combining the matrix and the fracture contributions, while the last two terms correspond to the outflow and inflow boundary contribution in (10).

It is well known that the system the system (11) leads in general to the oscillatory solutions and does not preserve the maximum principle (see e.g. [30]). This is mainly due to the presence of the negative off-diagonal terms in the matrix $\widetilde{K}$. In order to obtain a non-oscillatory discretization of (7) we will modify (11) along the following axes. First, we replace the mass matrix by it's lumped approximation and introduce some particular treatment of the boundary terms that, again, can be interpreted as a sort of lumping. As the result the system (11) will be replaced by the system (12) below, which can be interpreted as a conservative FV-FE method. Secondly the transport operator $\widetilde{K}$ will be turned into a monotone one by means of the AFC method, this procedure will be discussed in Section 3.4.

3.3 FV-FE discretization

Let $L(\mathbb{R}^N)$ denote the set of real N-by-N matrices and let $L_d(\mathbb{R}^N) \subset L(\mathbb{R}^N)$ denote the subset of diagonal matrices. We introduce the following "row sum" operator RS from $L(\mathbb{R}^N)$ onto $L_d(\mathbb{R}^N)$, such that for any $A \in L(\mathbb{R}^N)$ the elements of $D = RS(A)$ are given by

$$d_{ij} = \begin{cases} \sum_k a_{ik}, & \text{if} \quad i = j, \\ 0 & \text{if} \quad i \neq j. \end{cases}$$

In other words the diagonal of $RS(A)$ is made of the a row sums of A.

Using those notations the lumped mass matrix M is defined by $M = RS(\widetilde{M})$; more specifically the elements of M satisfy

$$m_{ii} = \frac{1}{d+1}\sum_{T\in\mathcal{T}_i} \phi_m|_T|T| + \frac{1}{d}\sum_{\sigma\in\mathcal{F}_i\cap\mathcal{F}_\Gamma} (\phi_f d_f)|_\sigma|\sigma|.$$

Let $S = RS(\widetilde{K})$, we remark that the elements of S satisfy

$$s_{ii} = \int_{\Omega_m} \nabla\eta_i \cdot \mathbf{q}_{m,h}\,\mathrm{d}\mathbf{x} + \int_{\Gamma} \nabla_\tau\eta_i \cdot \mathbf{q}_{f,h}\,\mathrm{d}\sigma(\mathbf{x}),$$

where s_{ii} can be interpreted as the total Darcy flux to the node i. Note that in view of (9) we have that $s_{ii} = 0$ for all $i \in \mathcal{N} \setminus \mathcal{N}_D$. For $i \in \mathcal{N}_D$ this quantity is non-zero in general, and one can distinguish between the outflow and the inflow boundary nodes based on the sign of s_{ii}.

Introducing the diagonal matrices $S^+ = \max(S, 0)$ and $S^- = \min(S, 0)$ (where max and min are applied element-wise) we replace the system (11) by the following one

$$M\frac{\mathrm{d}c}{\mathrm{d}t} = \widetilde{K}c - \left(S^+c + S^-c_D\right). \tag{12}$$

Below we give an interpretation of (12) and (9) in terms of the FV method. In particular, we will show that the system (12) can be expressed in the following conservative form

$$m_{ii}\frac{\mathrm{d}c_i}{\mathrm{d}t} = \sum_{j\in\mathcal{N}_i\setminus\{i\}} f_{ij} - f_{i,D} \qquad \forall i \in \mathcal{N}, \tag{13}$$

where $f_{ij} = -f_{ji}$ are the edge fluxes from the neighboring nodes to the node i and $f_{i,D}$ is the nodal boundary flux from the node i. Similarly, the problem (9) can be written as a set of local conservation equations for "non-Dirichlet" nodes

$$\sum_{j\in\mathcal{N}_i\setminus\{i\}} q_{ij} = 0 \qquad \forall i \in \mathcal{N}\setminus\mathcal{N}_D, \tag{14}$$

where $q_{ij} = -q_{ji}$ are the edge Darcy fluxes form the neighboring nodes to the node i.

Since $\nabla\eta_i$ and $\mathbf{q}_{m,h}$ are element-wise constant, using $\sum\limits_{j\in\mathcal{N}_T}(\nabla\eta_j)|_T = 0$ for any $T \in \mathcal{T}$ and denoting $c_T = \dfrac{1}{d+1}\sum\limits_{j\in\mathcal{N}_T} c_j$, we obtain for any $i \in \mathcal{N}$

$$\begin{aligned}
\int_{\Omega_m} \nabla\eta_i \cdot c_h\mathbf{q}_{m,h}\,\mathrm{d}\mathbf{x} &= \sum_{T\in\mathcal{T}_i} c_T \int_T \nabla\eta_i\cdot\mathbf{q}_{m,h}\,\mathrm{d}\mathbf{x} \\
&= -\sum_{T\in\mathcal{T}_i} c_T \int_T \nabla\eta_i\cdot\Lambda_m|_T \sum_{j\in T}(\nabla\eta_j p_j)\,\mathrm{d}\mathbf{x} \\
&= -\sum_{T\in\mathcal{T}_i} c_T \left(\int_T \sum_{j\in T}(\nabla\eta_i\cdot\Lambda_m|_T\nabla\eta_j)\,\mathrm{d}\mathbf{x}\right)(p_j - p_i).
\end{aligned} \tag{15}$$

Denoting

$$\beta_{ij}^T = -\int_T \nabla\eta_i\cdot\Lambda_m|_T\nabla\eta_j\,\mathrm{d}\mathbf{x},$$

and changing the sum order in the last term in (15) we get

$$\int_{\Omega_m} \nabla\eta_i\cdot c_h\mathbf{q}_{m,h}\,\mathrm{d}\mathbf{x} = \sum_{j\in\mathcal{N}_i\setminus\{i\}}\sum_{T\in\mathcal{T}_i\cap\mathcal{T}_j} c_T\beta_{ij}^T(p_j - p_i). \tag{16}$$

Similarly, for any $i \in \mathcal{N}_\Gamma$ we have

$$\int_\Gamma \nabla_\tau\eta_i\cdot c_h\mathbf{q}_{f,h}\,\mathrm{d}\sigma(\mathbf{x}) = \sum_{j\in\mathcal{N}_i\cap\mathcal{N}_\Gamma\setminus\{i\}}\sum_{\sigma\in\mathcal{F}_i\cap\mathcal{F}_j} c_\sigma\beta_{ij}^\sigma(p_j - p_i). \tag{17}$$

with $c_\sigma = \dfrac{1}{d}\sum\limits_{j\in\mathcal{N}_\sigma} c_j$ and

$$\beta_{ij}^\sigma = -\int_\sigma \nabla_\tau\eta_i\cdot(d_f\Lambda_f)\,|_\sigma\nabla_\tau\eta_j\,\mathrm{d}\mathbf{x}.$$

Let

$$q_{ij} = \sum_{T\in\mathcal{T}_i\cap\mathcal{T}_j}\beta_{ij}^T(p_j - p_i) + \sum_{\sigma\in\mathcal{F}_i\cap\mathcal{F}_j\cap\mathcal{F}_\Gamma}\beta_{ij}^\sigma(p_j - p_i). \tag{18}$$

for any $i \in \mathcal{N}$ and $j \in \mathcal{N}_i\setminus\{i\}$. Clearly $q_{ij} = -q_{ji}$, and, in view of (16), (17) and (18), the pressure problem (9) can be expressed in the conservative form (14).

Let us show that (12) can be written as (13). We define the nodal boundary flux as

$$f_{i,D} = c_i\max(0, s_{ii}) + c_{D,i}\min(0, s_{ii}) \tag{19}$$

and the edge fluxes as

$$f_{ij} = \sum_{T\in\mathcal{T}_i\cap\mathcal{T}_j} c_T\beta_{ij}^T(p_j - p_i) + \sum_{\sigma\in\mathcal{F}_i\cap\mathcal{F}_j\cap\mathcal{F}_\Gamma} c_\sigma\beta_{ij}^\sigma(p_j - p_i). \tag{20}$$

One can observe that, in view of (16), (17), (19) and (20), the system (12) can be expressed in the conservative form (13).

3.4 Algebraic flux correction

So far we have replaced (11) by (12), which we have interpreted as a FV discretization. We will now introduce a monotone version of (12) by performing the algebraic flux correction of $\widetilde{K}$. To do that we add some amount of solution dependent edge diffusion. As the result, the system (12) will be replaced by the following one

$$M\frac{\mathrm{d}c}{\mathrm{d}t} = \left(\widetilde{K} + \overline{D}(c)\right)c - \left(S^{+}c + S^{-}c_D\right), \tag{21}$$

where $\overline{D}$ is the nonlinear mapping from $\mathbb{R}^N$ to $L(\mathbb{R}^N)$ satisfying $\overline{d}_{ij}(c) = \overline{d}_{ji}(c) \geq 0$ for $i \neq j$ and $\overline{d}_{ii}(c) = -\sum_{j\neq j} \overline{d}_{ij}(c)$. The solution dependent diffusion matrix $\overline{D}(c)$ will provide a limited amount of numerical diffusion allowing for the discrete maximum principle to hold. Note that in view of the zero row sum property of $\overline{D}$ we have

$$\left(\overline{D}(c)c\right)_i = \sum_j \overline{d}_{ij}(c)(c_j - c_i), \tag{22}$$

and we remark that, since $\overline{d}_{ij}(c) = \overline{d}_{ji}(c)$, the extra diffusion term in (21) does not affect the conservativity of the scheme.

This discretization design relies on the following proposition, which states the sufficient conditions under which a general semi-implicit discretization guarantees the local and the global discrete maximum principles.

Proposition 3.1 (Discrete maximum principle) *Let N be a positive integer, let $A, B \in L(\mathbb{R}^N)$ and let $C \in L(\mathbb{R}^N)$ be a diagonal matrix with non-negative elements; we further assume that the row sums of A and B satisfy $RS(A) - RS(B) = C$. Let $u^0 \in \mathbb{R}^N$ and let $(g^n)_{n\geq 0}$ be a sequence of vectors from $\mathbb{R}^N$, we consider the following iterative scheme*

$$Au^{n+1} = Bu^n + Cg^n, \qquad n \geq 0. \tag{23}$$

For all $i \in \{1, \ldots, N\}$ we define

$$\widetilde{\mathcal{N}}_i = \{j \in \{1, \ldots, N\} | \, |a_{ij}| + |b_{ij}| > 0\}.$$

Assume that A is an M-matrix and that B is non-negative, then the iterates u_i^n satisfy the following global "in space" DMP

$$\min\left(\min_j u_j^n, \min_j g_j^n\right) \leq u_i^{n+1} \leq \max\left(\max_j u_j^n, \max_j g_j^n\right). \tag{24}$$

Moreover, the following local DMP also holds

$$\min_{k\in\{n,n+1\}}\left(\min_{j\in\widetilde{\mathcal{N}}_i\setminus\{i\}} u_j^k\right) \leq u_i^{n+1} \leq \max_{k\in\{n,n+1\}}\left(\max_{j\in\widetilde{\mathcal{N}}_i\setminus\{i\}} u_j^k\right) \tag{25}$$

for all i such that $c_{ii} = 0$.

Proof: The proof is rather standard and is given here for the sake of completeness. A somewhat similar result can be found for example in [30]. Let us first recall that the matrix A is said to be an M-matrix if A is invertible, A^{-1} is non-negative and $a_{ij} \leq 0$ for $i \neq j$. We also remark that the diagonal elements of an M-matrix are strictly positive [40, 2.4.8]. Let w be a vector in $\mathbb{R}^N$ with equal components, setting $v^k = u^k - w$ for $k \geq 0$ we obtain

$$Av^{n+1} + RS(A)w = Bv^n + RS(B)w + Cg^n$$

and

$$Av^{n+1} = Bv^n + C(g^n - w). \tag{26}$$

To prove the global DMP, we set for all components of w to

$$\min\left(\min_j u_j^n, \min_j g_j^n\right)$$

providing that $v^n \geq 0$ and $g^n - w \geq 0$. Since A^{-1} is non-negative we obtain $v^{n+1} \geq 0$ which proves the lower bound in (24). The upper bound is obtained similarly.

In order to prove (25) we consider some $i \in \{1, \dots, N\}$ such that $c_{ii} = 0$. The row i of the system (26) reads as

$$a_{ii} v_i^{n+1} = \sum_{j \neq i} (-a_{ij}) v_j^{n+1} + \sum_j b_{ij} v_j^n. \tag{27}$$

Setting all components of w to

$$\min_{k \in \{n, n+1\}} \left(\min_{j \in \widetilde{\mathcal{N}}_i \setminus \{i\}} u_j^k \right)$$

we observe that $v_j^k \geq 0$ for all $j \in \widetilde{\mathcal{N}}_i$ and $k \in \{n, n+1\}$, this implies that the right-hand-side of (27) is non-negative in view of the assumption on A and B. Since $a_{ii} > 0$ we deduce that $v_i^{n+1} \geq 0$, which in turn implies the lower bound in (25). The upper bound is obtained similarly. □

We can think about (23) as of a discretization of some evolutionary PDE. In that case the term g^n can be interpreted as the variable in time Dirichlet boundary data associated with the discretization nodes i satisfying $c_{ii} > 0$; the initial condition is given by u^0. Under such interpretation Proposition 3.1 implies that the local (in space) extrema decrease over time, while the global (in space and time) extrema are reached at the boundary of the space-time domain.

For the sake of clarity we first present the AFC method applied to the combined matrix-fracture transport. Alternatively, one may want to treat the fracture and the matrix transport terms separately, in that case the transport operator $\widetilde{K} = \widetilde{K}_m + \widetilde{K}_f$ has to be replaced with $\sum_{\alpha=m,f} (\widetilde{K}_\alpha + \overline{D}_\alpha(c))$, where the the diffusive correction is computed for the matrix and fracture domains separately. This version of the method will be discussed in Section 3.5.2 below in the context of a semi-implicit discretization.

We recall below the algebraic flux correction method as it was presented in [25], for the review of more recent literature we refer to [4] and [30]. The first step is to design the lower order linear transport operator whose matrix L would have non-negative off-diagonal elements. Such low-order operators involving upwind flux discretization can be obtained using for example a FV-FE approach as in [33], [34], or [9]. Here instead, following the AFC methodology, we define the low-order discretization L in a purely algebraic way, that is solely based on the coefficients of $\widetilde{K}$.

To begin with we identify the "divergence free" part of $\widetilde{K}$. As before we denote $S = RS(\widetilde{K})$ and we defined by $K = \widetilde{K} - S$ which has a zero row sums. The low-order transport operators L is obtained from K by adding the minimal amount of artificial diffusion that allows L to have only non-negative off-diagonal elements. Let $D \in L(\mathbb{R}^N)$ be a symmetric matrix, whose elements are given by

$$d_{ij} = d_{ji} = \max(0, -k_{ij}, -k_{ji}) \quad \text{for } i \neq j \quad \text{and} \quad d_{ii} = -\sum_{j \neq i} d_{ij},$$

We set $L = K + D$ and we introduce the nonlinear edge diffusion operator in the form

$$\overline{D}(c) = D - U(c), \tag{28}$$

where $U(c)$ is a symmetric solution dependent matrix with non-negative off-diagonal coefficient and satisfying zero row sum property. The aim of U is to remove a certain of numerical diffusion introduced by D. In order to define $U(c)$ we first express, using zero row sum property K, the total flux to the node $i \in \mathcal{N}$ as

$$(Kc)_i = \sum_{j \neq i} \min(0, k_{ij})(c_j - c_i) + \sum_{j \neq i} \max(0, k_{ij})(c_j - c_i),$$

where the first term in the right-hand-side is anti-diffusive in nature and is responsible for numerical instability, while the second term is diffusive and is not problematic. For $i \in \mathcal{N}$ let us denote by $Q_i^\pm$ the total diffusive flux to and from the node i, that is

$$Q_i^+ = \sum_{j \neq i} \max(0, k_{ij}) \max(0, c_j - c_i) \qquad \text{and} \qquad Q_i^- = \sum_{j \neq i} \max(0, k_{ij}) \min(0, c_j - c_i). \tag{29}$$

Similarly we define the inflow and outflow anti-diffusive contributions

$$P_i^+ = \sum_{j \neq i} \min(0, k_{ij}) \min(0, c_j - c_i) \qquad \text{and} \qquad P_i^- = \sum_{j \neq i} \min(0, k_{ij}) \max(0, c_j - c_i). \tag{30}$$

Following [25] we correct the inflow and outflow anti-diffusive separately. Let $\Phi(r)$ denote some standard symmetric flux limiter function, in the numerical experiment (Section 4) we present the results for the minmod and superbee limiters, for which we have the following expressions

Minmod: $\Phi(r) = \max(0, \min(r, 1))$;

Superbee: $\Phi(r) = \max(0, \min(2r, 1), \min(r, 2))$.

For any edge (i, j) let us assume for the moment and without loss of generality that it is oriented such $l_{ji} \geq l_{ij}$. In other words i is an upstream node with respect to j (in the sense of algebraic upwinding defined by L). Denoting $R_i^{\pm} = \dfrac{Q_i^{\pm}}{P_i^{\pm}}$ and using the convention $l_{ji} \geq l_{ij}$ we define the the coefficients of U by

$$u_{ij}(c) = \begin{cases} \min(\Phi(R_i^+)d_{ij}, l_{ji}), & c_i - c_j \geq 0 \\ \min(\Phi(R_i^-)d_{ij}, l_{ji}), & c_i - c_j < 0, \end{cases} \qquad \text{and} \qquad u_{ji}(c) = u_{ij}(c). \tag{31}$$

Remark 3.1 *In view of* (28)*, and using* $\widetilde{K} = K + S$ *and* $L = \widetilde{K} + D$ *we can can be expressed the system* (21) *in the following form*

$$M\frac{\mathrm{d}c}{\mathrm{d}t} = (S + \mathcal{K}(c))\, c - \left(S^+ c + S^- c_D\right),$$

with $\mathcal{K}(c)$ *satisfying*

$$(\mathcal{K}(c)c)_i = \sum_j l_{ij}(c_j - c_i) - \sum_j u_{ij}(c_j - c_i). \tag{32}$$

We wish to stress out that the solution dependent coefficients $l_{ij} - u_{ij}$ *in* (32) *may still be negative. However, the definition* (31) *guaranties that for any* c *there exists a zero row sum matrix* $\mathcal{K}^\star(c)$ *with non-negative off-diagonal elements such that* $\mathcal{K}(c)c = \mathcal{K}^\star(c)c$*. Indeed, let* $\mathcal{N}_i^+ = \{j \in \mathcal{N}_i | l_{ij} \geq l_{ij}\}$ *and* $\mathcal{N}_i^- = \{j \in \mathcal{N}_i | l_{ij} < l_{ji}\}$*, we rewrite* (32) *as*

$$(\mathcal{K}(c)c)_i = \sum_{j \in \mathcal{N}_i^+} (l_{ij} - u_{ij})(c_j - c_i) + \sum_{j \in \mathcal{N}_i^-} (l_{ij} - u_{ij})(c_j - c_i). \tag{33}$$

In view of (31) *we have that* $u_{ij} \leq \max(l_{ij}, l_{ji})$*, which implies that the last term in* (33) *is diffusive, in the sense that* $l_{ij} - u_{ij} \geq 0$ *for* $j \in \mathcal{N}_i^+$*. Now let us show that, for* $j \in \mathcal{N}_i^-$ *the anti-diffusive flux* $-u_{ij}(c_j - c_i)$ *can be expressed as a sum of the diffusive ones, that is*

$$-u_{ij}(c_j - c_i) = \sum_k u_{ik}^{\star,j}(c_k - c_i), \qquad u_{ij}^{\star,j} \geq 0. \tag{34}$$

If $d_{ij} = 0$ *there is nothing to prove, so let us assume that* $d_{ij} > 0$*. Let us first assume that* $c_i - c_j \geq 0$*. Using the "symmetry" of the flux limiter, that is* $\Phi(r) = r\Phi(1/r)$ *for any* $r \geq 0$*, we deduce from* (31) *that*

$$u_{ij}(c_i - c_j) = a_{ij}^+ R^+ d_{ij} \max(0, c_i - c_j)$$

with $a_{ij}^+ = \Phi(1/R_i^+) \min(1, l_{ji}/(d_{ij}\Phi(R_i^+))) \geq 0$*. Using the expression of* $R_i^+ = \dfrac{Q_i^+}{P_i^+}$ *and* (29) *we obtain*

$$u_{ij}(c_i - c_j) = a_{ij}^+ \frac{d_{ij}\max(0, c_i - c_j)}{P_i^+} \sum_k \max(0, k_{ik}) \max(0, c_k - c_i).$$

Denoting by $H^+(x)$ *the Heaviside function we obtain that the coefficients* $u_{ik}^\star$ *given by*

$$u_{ik}^{\star,j} = a_{ij}^+ \frac{d_{ij}\max(0, c_i - c_j)}{P_i^+} H^+(c_k - c_i)$$

and are clearly positive in view of the definition of (30)*. The proof of* (33) *for the case* $c_i - c_j < 0$ *is similar.*

To conclude, we have shown that that $\mathcal{K}(c)c$ *can be expressed as* $\mathcal{K}^\star(c)c$*, where the matrix* $\mathcal{K}^\star(c)$ *has non-negative off-diagonal elements and zero row sums; more precisely we have*

$$(\mathcal{K}^\star(c)c)_i = \sum_{j \in \mathcal{N}_i^+} (l_{ij} - u_{ij})(c_j - c_i) + \sum_{k \in \mathcal{N}_i \setminus \{i\}} u_{ik}^\star (c_k - c_i)$$

with $u_{ik}^\star = \sum_{j \in \mathcal{N}_i^-} u_{ik}^{\star,j} \geq 0$*, and where* $l_{ij} - u_{ij}(c) \geq 0$ *for all* $j \in \mathcal{N}_i^+$*.*

3.5 Time discretization

3.5.1 Explicit discretization

Let us first present a simple forward Euler method. Let $\Delta t > 0$, we consider the following explicit scheme

$$M\frac{c^{n+1}-c^n}{\Delta t} = \left(\widetilde{K} + \overline{D}(c^n)\right)c^n - \left(S^+c^{n+1} + S^-c_D\right). \tag{35}$$

We refer to the discretization (35) as to $o2$-explicit scheme. In addition, we consider a low-order linear version of this discretization where the $\overline{D}(c^n)$ is replaced by D. This scheme denoted as $o1$-explicit is defined by

$$M\frac{c^{n+1}-c^n}{\Delta t} = \left(\widetilde{K} + D\right)c^n - \left(S^+c^{n+1} + S^-c_D\right). \tag{36}$$

Let us show that the linear scheme (36) satisfies the assumptions of Proposition 3.1 under some CFL-like condition on Δt. We can write (36) as

$$Ac^{n+1} = Bc^n - S^-c_D$$

with

$$A = M/\Delta t + S^+ \qquad \text{and} \qquad B = M/\Delta t + \widetilde{K} + D.$$

Since $\widetilde{K} + D = L + S$, we have

$$B = M/\Delta t + L + S.$$

Clearly A is an M-matrix and we have that $RS(A) - RS(B) = -S^-$; in addition the off-diagonal elements of B are non-negative. It remains to insure that B has a non-negative diagonal. That can be guarantied by the following the CFL-like condition

$$\Delta t \leq \max_{i\in\mathcal{N}} \frac{m_{ii}}{\max(0, |l_{ii}| - s_{ii})}, \tag{37}$$

where $|l_{ii}| - s_{ii}$ can be expressed as $-\widetilde{k}_{ii} - d_{ii}$.

3.5.2 Semi-implicit discretization

Due to the high permeability contrast between the matrix and the fracture domains we expect the transport in the fracture network to occurs at the time scale much smaller than the one associated with the matrix. This motivates us to use a separate time discretization in the matrix and fracture domains.

In order to perform the AFC in the matrix and the fracture transport operators separately we identify the "divergence free" parts of the operators $\widetilde{K}_m$ and $\widetilde{K}_f$. For $\alpha = m, f$, let $S_\alpha = RS(\widetilde{K}_\alpha)$ and $K_\alpha = \widetilde{K}_\alpha - S_\alpha$, where K_α satisfy the zero row sum property. We consider the following semi-implicit time discretization of (21)

$$M\frac{c^{n+1}-c^n}{\Delta t} = \left(\widetilde{K}_m + \overline{D}_m(c^n)\right)c^n + \left(\widetilde{K}_f + D_f\right)c^{n+1} - \left(S^+c^{n+1} + S^-c_D\right), \tag{38}$$

where D_f and $\overline{D}_m$ are the edge diffusion operators build upon K_f and K_m respectively. Note that the scheme (38) relies on the linear low-order approximation approximation in the fracture domain. Alternatively one can replace the operator D_f by the nonlinear one $\overline{D}_f(c^{n+1})$ in which case the scheme would require to solve a nonlinear system at each time step [25], [20], [29], [21], [31]. However, since we are interested in using large time steps that would typically lead to the fracture CFL number much large than 1, it is not clear if such higher-order nonlinear implicit scheme would improve the accuracy. The comparison of the mixed-order scheme (38) with the fully explicit higher-order method (35) is presented in Section 4.1. The results of the numerical experiment suggest that the mixed-order scheme is sufficiently accurate at least at the matrix time scale.

The mixed-order semi-implicit discretization (38) is referred to as $o1$-$o2$-semi-implicit scheme. We also consider a low-order linear version of this scheme obtained by replacing $\overline{D}_m$ with D_m. This scheme, denoted as $o1$-semi-implicit, is defined by

$$M\frac{c^{n+1}-c^n}{\Delta t} = \left(\widetilde{K}_m + D_m\right)c^n + \left(\widetilde{K}_f + D_f\right)c^{n+1} - \left(S^+c^{n+1} + S^-c_D\right). \tag{39}$$

Let us investigate the monotonicity condition of the linear scheme (39). We will show that (39) satisfies the assumptions of Proposition 3.1 under some condition on Δt. We express (39) as

$$Ac^{n+1} = Bc^n - S^- c_D$$

with

$$A = \frac{M}{\Delta t} - \widetilde{K}_f - D_f + S^+ \qquad \text{and} \qquad B = \frac{M}{\Delta t} + \widetilde{K}_m + D_m.$$

Since $\widetilde{K}_\alpha + D_\alpha = L_\alpha + S_\alpha$ with $\alpha = m, f$, and using $S = S^+ + S^- = S_f + S_m$, we have

$$A = \frac{M}{\Delta t} - L_f + S_m - S^- \qquad \text{and} \qquad B = \frac{M}{\Delta t} + L_m + S_m.$$

Since $RS(L_\alpha) = 0$ for $\alpha = m, f$ we deduce that

$$RS(A) - RS(B) = -S^-.$$

Next, the off-diagonal elements of B are non-negative since $b_{ij} = l_{m,ij} \geq 0$ for $i \neq j$, while the diagonal elements of B satisfy

$$b_{ii} = \frac{m_{ii}}{\Delta t} + l_{m,ii} + s_{m,ii}.$$

The non-negativity of b_{ii} can be insured by the condition

$$\Delta t \leq \max_{i \in \mathcal{N}} \frac{m_{ii}}{\max(0, |l_{m,ii}| - s_{m,ii})}. \tag{40}$$

It turns out that the condition (40) is also "almost sufficient" to insure that A is an M-matrix. It follows from (40) that

$$\frac{m_{ii}}{\Delta t} + s_{m,ii} \geq 0, \tag{41}$$

where the inequality in (41) is strict if either (40) is strict, or if $|l_{m,ii}| > 0$, for all i, which roughly speaking corresponds to some nontrivial matrix flow. Note that $a_{ij} = -l_{f,ij} \leq 0$ for $i \neq j$. Since L_f has zero row sums and since $s_{ii}^- \leq 0$, it follows from (41) that

$$a_{ii} \geq -l_{f,ii} = \sum_{j \neq i} l_{f,ij} = \sum_{j \neq i} |a_{ij}|. \tag{42}$$

This shows that A is diagonal dominant. Now, assume that either $|l_{m,ii}| > 0$ for all i or that the inequality (40) is strict. This implies that (41) holds with the strict inequality. In turn, the first inequality in (42) is also strict, which implies that A is strictly diagonally dominant and therefore is an M-matrix (see [40, 2.4.14]). Alternatively, the M-matrix property can be established assuming some nontrivial fracture flow, that is $|l_{f,ii}| > 0$ for all i, and a nonempty inflow boundary, that is $s_{ii}^- > 0$ for at least one i, which would imply that A is irreducibly diagonal dominant and that $a_{ii} > 0$ for all i. Let us remark that $|l_{m,ii}| - s_{m,ii} = -(\widetilde{k}_{m,ii} + d_{m,ii})$ and that the CFL-like condition (40) only involve the matrix discretization parameters and does not depends on the fast fracture flow.

Remark 3.2 *In view of Remark 3.1 and proceeding as above one can show that the schemes* (35) *and* (38) *satisfy the DMP under some appropriate condition on the time step. However deriving a sharp estimate on such stable time step is a delicate matter. In the numerical experiment presented below the choice of the time step for the nonlinear schemes* (35) *and* (38) *will be again based on* (37) *and* (40) *respectively.*

4 Numerical experiment

In this section we present two numerical experiments. The first test case presented in Section 4.1 allows for the analytical solution, which enables us to evaluate the numerical error and the experimental convergence rate of the schemes. In particular we will compare the performance of the mixed-order semi-implicit scheme (38) with the fully explicit high-order one (35). It results that at the large time scale the discretization (38) provides a sufficiently accurate solution, while, compared to (35), allowing for much larger time steps. In the second test case presented in Section 4.2 we compare the semi-implicit methods in the context of a realistic DFM model. As expected, compared to the $o1$-semi-implicit scheme, the solution produced by the mixed-order is much sharper and detailed. In Section 4.2 we also investigate the benefits of treating a small portion of high CFL matrix elements with the implicit time discretization. We show

that assigning of a small portion of the matrix elements to the implicit zone allows to increase the stable time step by few orders of magnitude without affecting the overall solution quality.

All numerical simulations are performed on conforming triangular meshes that are generated by Triangle software [43]. The stable time step Δt_{stab} is computed based on (37) for the explicit discretization and on (40) for the semi-implicit ones. As discussed above the provable CFL condition for the nonlinear schemes (35) and (38) is not available, as the rule of thumb we choose the actual time step to be smaller than $0.5\Delta t_{stab}$ for all discretization. This seems to be sufficient since we have not encountered the violation of the global DMP in the simulations. Let T_f denote some positive final simulation time, for the sake of constancy when evaluating the numerical error we also choose the actual time step smaller than $T_f/100$. More precisely we define the time step as follows: let N be a number of time steps given by

$$N_T = \min\{k \in \mathbb{N} |\, k \min(\Delta t_{max}, 0.5\Delta t_{stab}) \geq T_f\},$$

we, then, set $\Delta t = T_f/N_T$.

4.1 Single fracture analytical test case

We consider the numerical test case with a single fracture from taken from [10] and [48], for which the solution can be computed analytically. The geometry of the test case is represented on Figure 2. Let $\Omega = (0,1)^2$, the fracture domain is defined by $\Gamma = \{(x, y \in \Omega) |\, y = 1/4 + x\tan\theta\}$, with $\theta = \pi/4$, as before we set $\Omega_m = \Omega \setminus \Gamma$. The pressure field is given by $p(x,y) = 1 - x$. The initial tracer concentration is zero and boundary conditions are given by $c_m(x,y,t) = 1$ on $\partial\Omega_D^- = \overline{\Omega_m} \cap \{x = 0\}$ and $c_f(x,y,t) = 1$ on $\Gamma_D^- = \overline{\Gamma} \cap \{(0, 1/4)\}$ for $t \in (0, T_f)$, where the final simulation time is set to $T_f = 0.5$. We refer to [10] for the closed form of the solution.

Following [48] we set $\phi_m = \phi_f = 1$, $d_f = 0.01$, we set $\Lambda_m = 1$, and we consider two values of the fracture tangential permeability $\Lambda_f = 20$ (low permeability contrast) and $\Lambda_f = 2000$ (high permeability contrast). Because of the permeability contrast the solution of the transport

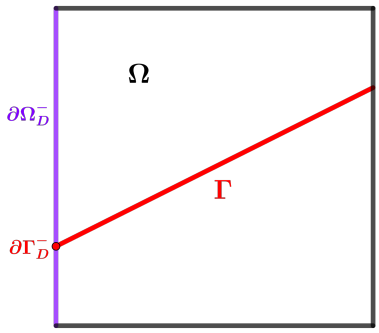

Figure 2: Matrix and fracture domains for the analytical test case.

problem involves two time scales - the fast fracture time scale and the slower matrix one. The fast fracture filling process is characterized by the time $\tau_f = \frac{1}{\Lambda_f \cos(\theta)^2}$, which is the time required for the concentration front to reach the right outflow boundary. For $t > \tau_f$ the fracture equation (5) is essentially stationary and the fracture concentration profile is controlled by the matrix-fracture exchanges. We illustrate this dynamics by Figure 3 that reports the fracture solution profiles for the small times (comparable to τ_f) and the large times (comparable to T_f). Note that for $t \geq \tau_f$ the fracture concentration is continuous. To further illustrate the time scale contrast we report at Figure 4 the average fracture concentration as the function of time. Figures 5 and 6 show the exact matrix solution at $t = \tau_f$ and $t = T_f$.

For this test case we use four different triangular meshes with the total number dofs ranging from 100 to about $100\,10^3$, the characteristics of the meshes are reported in Table 1. Depending on the value of Λ_f the fully explicit time discretizations (35) and (36) require the time step which few times or few hundred times smaller than the stable time step of the semi-implicit methods (38) and (39). The time discretization parameters are reported in Tables 2. For the case $\Lambda_f = 20$ we present the simulation results and the experimental convergence analysis for both explicit and semi-implicit schemes; more precisely we consider $o1$-explicit and $o1$-semi-implicit, $o2$-explicit and the mixed-order $o1$-$o2$-semi-implicit discretizations. For the schemes using the second order discretization in the matrix domain we consider the minmod and the

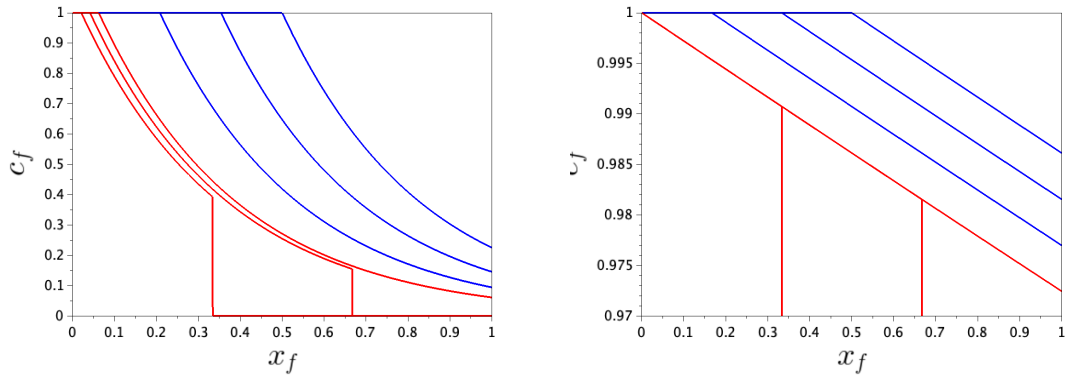

Figure 3: Exact solution in fracture domain for $\Lambda_f = 20$ (left) and $\Lambda_f = 2000$ (right). Red curves represent the solution profile at times $t = \frac{k}{3}\tau_f$, $k = 1, 2, 3$. Blue curves show the solution at times $t = \tau_f + \frac{k}{3}(T - \tau_f)$, $k = 1, 2, 3$. Fracture length is rescaled.

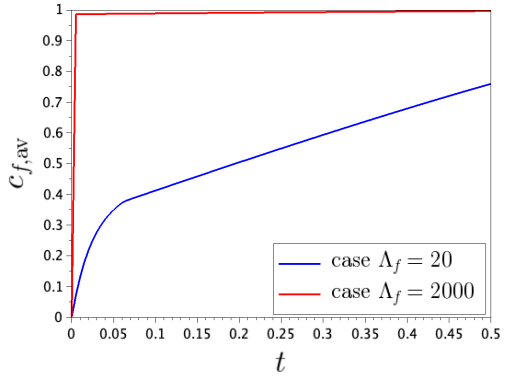

Figure 4: Average fracture concentration as the function of time for $\Lambda_f = 20$ and $\Lambda_f = 2000$.

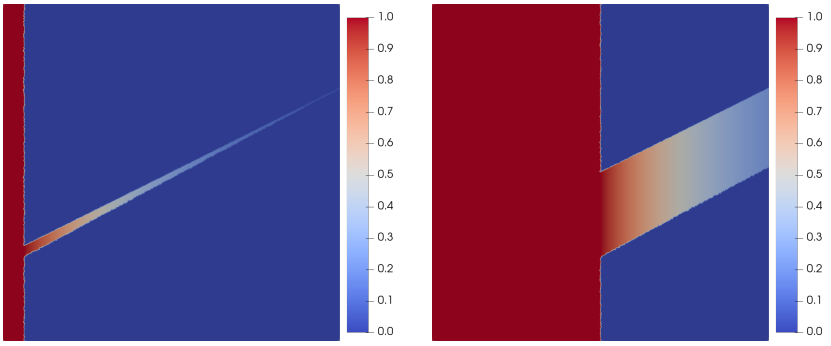

Figure 5: Exact solution in matrix domain for $\Lambda_f = 20$ at $t = \tau_f$ (left) and $t = T$ (right).

superbee limiters. Because of a strong CFL constraint in the high permeability contrast case $\Lambda_f = 2000$ we limit the numerical experiment to the family of semi-implicit methods.

Let $\overline{c}_m(\mathbf{x}, t)$ and $\overline{c}_f(\mathbf{x}, t)$ denote the exact matrix and fracture tracer concentration. For each mesh and all time steps n, we denote by $\overline{c}_\alpha^n$, $\alpha = m, f$, the standard nodal FE interpolation

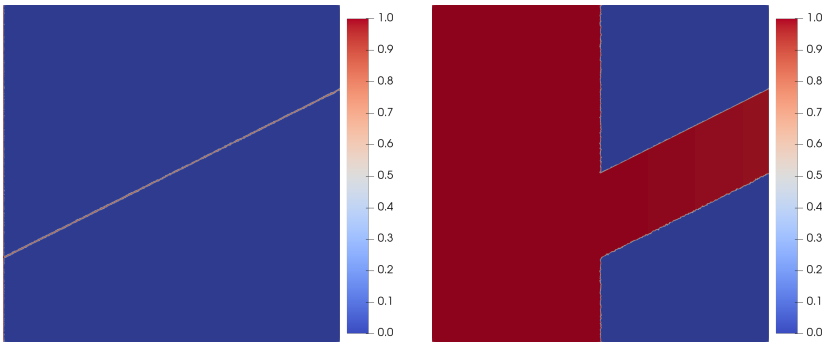

Figure 6: Exact solution in matrix domain for $\Lambda_f = 2000$ at $t = \tau_f$ (left) and $t = T$ (right).

Mesh	# triangles	# frac. faces	# dof mat.	# dof frac.
1	172	10	104	11
2	1600	31	854	32
3	16460	99	8371	100
4	163510	284	82267	285

Table 1: Space discretization parameters.

of $\overline{c}_\alpha(\cdot, n\Delta t)$ in matrix and fractured domains respectively, that is we set

$$\overline{c}_m^n(\mathbf{x}) = \sum_{i\in\mathcal{N}} \eta_i(\mathbf{x})\overline{c}_m(\mathbf{x}_i, n\Delta t) \qquad \text{and} \qquad \overline{c}_f^n(\mathbf{x}) = \sum_{i\in\mathcal{N}_\Gamma} \eta_i|_\Gamma(\mathbf{x})\overline{c}_f(\mathbf{x}_i, n\Delta t).$$

For each mesh and each discretization we compute the matrix and fracture relative L_1 space-time error as follows

$$err_m = \frac{\sum_n \int_\Omega |c^n - \overline{c}_m^n| \, \mathrm{d}\mathbf{x}}{\sum_n \int_{\Omega_m} |\overline{c}_m^n| \, \mathrm{d}\mathbf{x}} \qquad \text{and} \qquad err_f = \frac{\sum_n \int_\Gamma d_f |c^n - \overline{c}_f^n| \, \mathrm{d}\sigma(\mathbf{x})}{\sum_n \int_\Gamma d_f |\overline{c}_f^n| \, \mathrm{d}\sigma(\mathbf{x})}.$$

4.1.1 Case $\Lambda_f = 20$

At Figure 15 we report the approximate solution at the final time T_f obtained on the fines mesh. The top row of the figure shows the results of the explicit time stepping schemes, while the bottom row reports the semi-implicit solutions. The amount of numerical diffusion reduces from left to right. The left column shows the solution obtained with the first-order space discretization, which introduces a large amount of numerical diffusion especially in the matrix domain. The smearing of the sharp matrix concentration front is largely reduced by the use of the second-order accurate schemes (middle and right columns). As expected the second-order scheme using superbee limiter (right column) produces the sharpest concentration fronts. At the same time one can notice some numerical artifacts introduced by this overcompressive scheme. Interestingly enough we observe that the semi-implicit discretizations leads to a slightly sharper fronts. It turns out that the mixed-order semi-implicit method even outperforms the second-order explicit one in terms of the L_1 space-time error (see Figure 7).

	Semi-implicit schemes			Explicit schemes $\Lambda_f = 20$			Explicit schemes $\Lambda_f = 2000$		
Mesh	$\Delta t_{stab} \times 10^3$	$\Delta t \times 10^3$	N_t	$\Delta t_{stab} \times 10^4$	$\Delta t \times 10^4$	N_t	$\Delta t_{stab} \times 10^6$	$\Delta t \times 10^6$	N_t
1	12.74	4.95	101	68.34	34.01	147	106.10	53.05	9425
2	4.97	2.48	202	17.41	8.7	575	22.94	11.47	43593
3	1.51	0.76	662	2.3	1.15	4350	2.46	1.23	407114
4	0.45	0.22	2247	0.75	0.37	13405	0.76	0.38	1309383

Table 2: Time discretization parameters.

Figure 16 shows the concentration profile in the fracture domain at the final time T_f. The results are reported for the finest mesh. At the matrix transport time scale the fracture transport equation (5) is almost stationary and the matrix-fracture exchange term plays a crucial role. For such time scale a correctly captured matrix solution would result in a accurate fracture concentration profile. All the schemes captures well the solution profile away from the middle of the fracture, which coincide with the matrix front location. Near $x = 0.5$ the shape of the solution is much better reproduced by $o2$-explicit and $o1$-$o2$-semi-implicit schemes, which is likely due to a smaller numerical diffusion in the matrix domain.

The figure 7 reports the relative L_1 matrix and fracture error as the function of the mesh size; the experimental order of convergence is reported in Tables 4 and 5. The explicit and the semi-implicit first-order methods lead to very similar results, both schemes achieve the order of convergence about 0.5 in the matrix domain and about 0.8 in the fracture (see Tables 4 and 5). The higher convergence order in the fracture domain can be attributed to the higher regularity of the solution for $t \geq \tau_f$.

The use of the schemes that are second-order accurate in the matrix domain allows to a significant improvement of the matrix solution (see Figure 7). The order of convergence is improved by minmod ($eoc \approx 0.64$) and superbee ($eoc \approx 0.92$) schemes using both fully explicit and semi-implicit formulations (see Tables 4 and 5). The error and the convergence rate in the fracture domain are also slightly improved. For all four schemes that are second-order accurate we observe the convergence rate close to 0.9. Note, that, in view of our time discretization method, we can not expect the convergence rate higher than 1. In this sense all four schemes perform almost optimally.

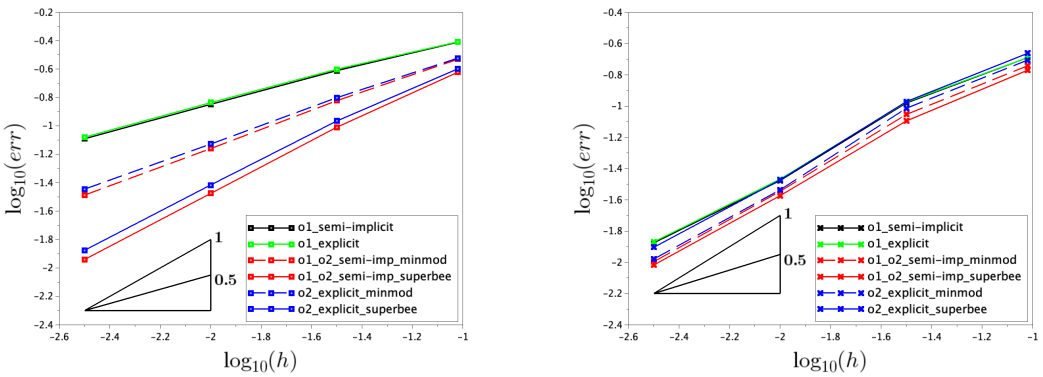

Figure 7: Relative L^1 space-time error as the function of the mesh size for matrix (left) and fracture (right) domains (case $\Lambda_f = 20$).

4.1.2 Case $\Lambda_f = 2000$

Because the fully explicit discretizations are subjects to a very restrictive time step constraint (see Table 2) we limit ourself to the family of semi-implicit methods. The figure 17 reports the approximate solution at the final time T_f obtained on the finest mesh, while at Figure 18 we report the solution profile in the fracture domain. As before the mixed-order scheme allows to reduce the numerical diffusion and leads to a more accurate solution both in matrix and fracture domains. We report on Figure 8 the relative L_1 space-time error for matrix and fracture domain as the function of the mesh size.

Regarding the error in the matrix domain the results obtained for this case are qualitatively similar to those of the case $\Lambda_f = 20$ for the family of semi-implicit discretizations. The observed order of convergence for the first order method is about 0.5 (see Table 6) which is the optimal one given the low regularity of the solution. The use of the second-order accurate discretization in the matrix domain allows to reduce the smearing of the solution fronts. As before, the most accurate results are obtained using the front preserving superbee limiter. We observe the convergence rate for the mixed-order schemes of 0.65 for minmod limiter and 0.9 for superbee limiter respectively (Table 6).

Because of a lower numerical diffusion in the matrix, the mixed-order semi-implicit discretizations allow, at least at the large time scale, for a more accurate representation of the solution profile (see Figure 18). On the other hand the performance of both first-order and the mixed-order semi-implicit schemes is almost identical in terms of L_1 space-time error in the fracture domain, the convergence rate is about 0.75. This behavior may probably be attributed to the fact that, due to its large time step, the semi-implicit schemes equally fail to represent the fast fracture dynamics occurring at the beginning of the simulation.

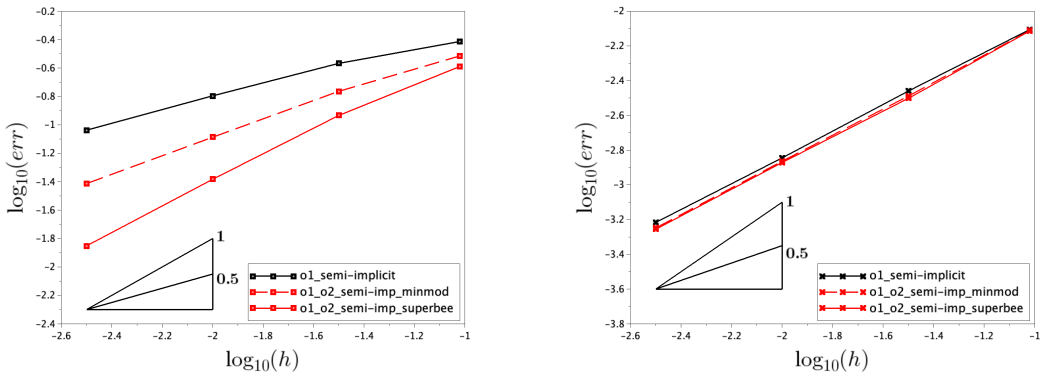

Figure 8: Relative L^1 space-time error as the function of the mesh size for matrix (left) and fracture (right) domains (case $\Lambda_f = 2000$).

4.2 Application to a complex fracture network

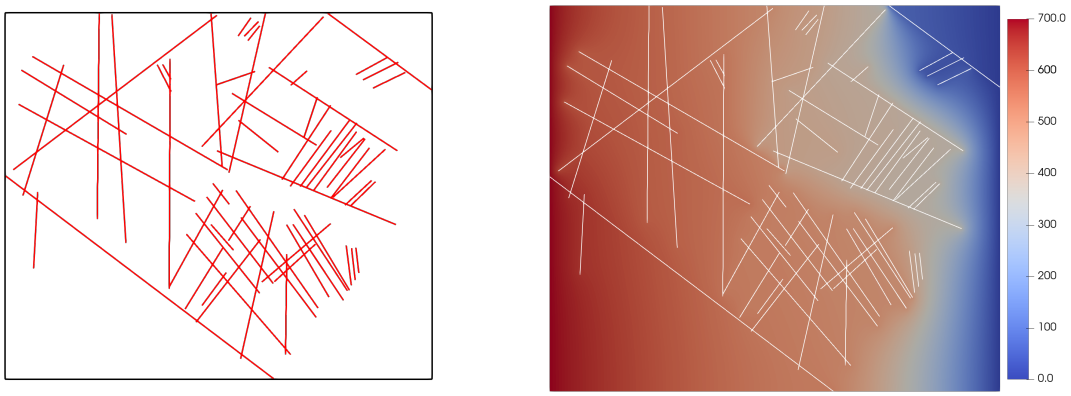

Figure 9: Left: flow domain and fracture network geometries. Right: matrix pressure field.

In this section we apply the first and the mixed-order semi-implicit methods to the test case involving a complex fracture network. The geometry of the fracture network is taken from [13] and is based on the outcrop observed at Sotra island. The flow domain, defined by $\Omega = (0, 700) \times (0, 600)$, and the fracture network is exposed on Figure 9. We set the following parameters $\phi_m = \phi_f = 1$, $d_f = 0.01$, $\Lambda_m = 1$ and $\Lambda_f = 2 \cdot 10^5$. The Dirichlet boundary conditions for the pressure problem are set on the left and the right boundaries of Ω; more specifically we set $p_D = 700$ on $\partial\Omega_D^- = \Omega \cap \{x = 0\}$ and $p_D = 0$ on $\partial\Omega_D^+ = \Omega \cap \{x = 700\}$. The remainder of the boundary is subject to zero Neumann boundary condition. The tracer transport is computed for the $t \in (0, T_f)$ with $T_f = 100$. The initial tracer concentration is zero both in matrix and the fracture domains, at the inflow boundary $\partial\Omega_D^-$ the concentration is set to 1.

We perform the computations using the triangular mesh having 138 672 triangular elements, 3896 fracture segments and a total of 69 778 nodal dofs. We compare the first order semi-implicit method with the mixed-order one using the superbee flux limiter. The time discretization based on the matrix stability condition is defined as in the previous test case and results in the time step $\Delta t = 8.88 \cdot 10^{-4}$.

We report on Figures 9 the matix pressure field and on Figures 11 the tracer concentration for $t = 10, 20, 40$ and 80. Although the results obtained by two methods are qualitatively similar, one can observe that the the mixed-order scheme produces a much sharper and detailed solution. A more quantitative error assessment is provided by Figure 10 which shows the weighted L_1 distance between the approximate solutions obtained by two schemes. More precisely, let $c^n_{o1}, c^n_{o1\text{-}o2} \in V_h$ denote the approximate solution at time t_n obtained by the scheme $o1$-semi-implicit and $o1$-$o2$-semi-implicit scheme respectively. We expose on the figure 10 the quantities

$$dist_m(t_n) = \frac{\displaystyle\int_{\Omega_m} |c^n_{o1} - c^n_{o1\text{-}o2}| \,\mathrm{d}\mathbf{x}}{\displaystyle\int_{\Omega_m} \mathrm{d}\mathbf{x}} \qquad \text{and} \qquad dist_f(t_n) = \frac{\displaystyle\int_{\Gamma} d_f |c^n_{o1} - c^n_{o1\text{-}o2}| \,\mathrm{d}\sigma(\mathbf{x})}{\displaystyle\int_{\Gamma} d_f \,\mathrm{d}\sigma(\mathbf{x})}.$$

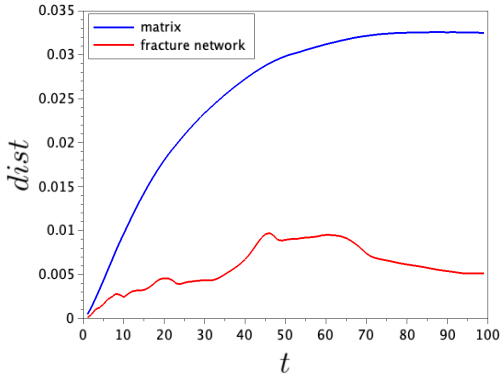

Figure 10: Weighed L_1 distance between the approximate solutions.

4.2.1 Implicit time stepping in high CFL matrix regions

In the context of high permeability contrast between matrix and fracture domains the use of the implicit time stepping in the fracture network makes the simulations computationally affordable. In this section we investigate the possibility of extending the implicit time stepping zone further in the matrix domain. More precisely, we identify the high CFL regions of the matrix domain to which we apply the implicit lower-order discretization. We show that treating a small portion of the matrix elements with the implicit time discretization allows to increase drastically the stable time step, while still preserving the accuracy.

The choice of the matrix elements to be assigned to the implicit zone will be based on the following element-wise parameter that characterizes the local CFL constraint

$$\xi_T = \frac{\sqrt{|T|}}{\|\mathbf{q}_{m,h}|_T\|_2}, \qquad \forall T \in \mathcal{T},$$

where $\mathbf{q}_{m,h}$ is defined by (8) and $\|\cdot\|_2$ denotes the standard Euclidean norm. For a given threshold value ξ we define the implicit and explicit zones as $\mathcal{T}_{imp}(\xi) = \{T \in \mathcal{T} | \, \xi_T \geq \xi\}$ and $\mathcal{T}_{exp}(\xi) = \mathcal{T} \setminus \mathcal{T}_{imp}(\xi)$. Based on this splitting of $\mathcal{T}$ we define the implicit and explicit matrix transport operators $\widetilde{K}_{m,imp}$ and $\widetilde{K}_{m,exp}$ that are associated with the FE bilinear forms

$$(\psi, c_m) \mapsto \sum_{T \in \mathcal{T}_{imp}(\xi)} \int_T c_m \nabla\psi \cdot \mathbf{q}_m \,\mathrm{d}\mathbf{x} \quad \text{and} \quad (\psi, c_m) \mapsto \sum_{T \in \mathcal{T}_{exp}(\xi)} \int_T c_m \nabla\psi \cdot \mathbf{q}_m \,\mathrm{d}\mathbf{x}.$$

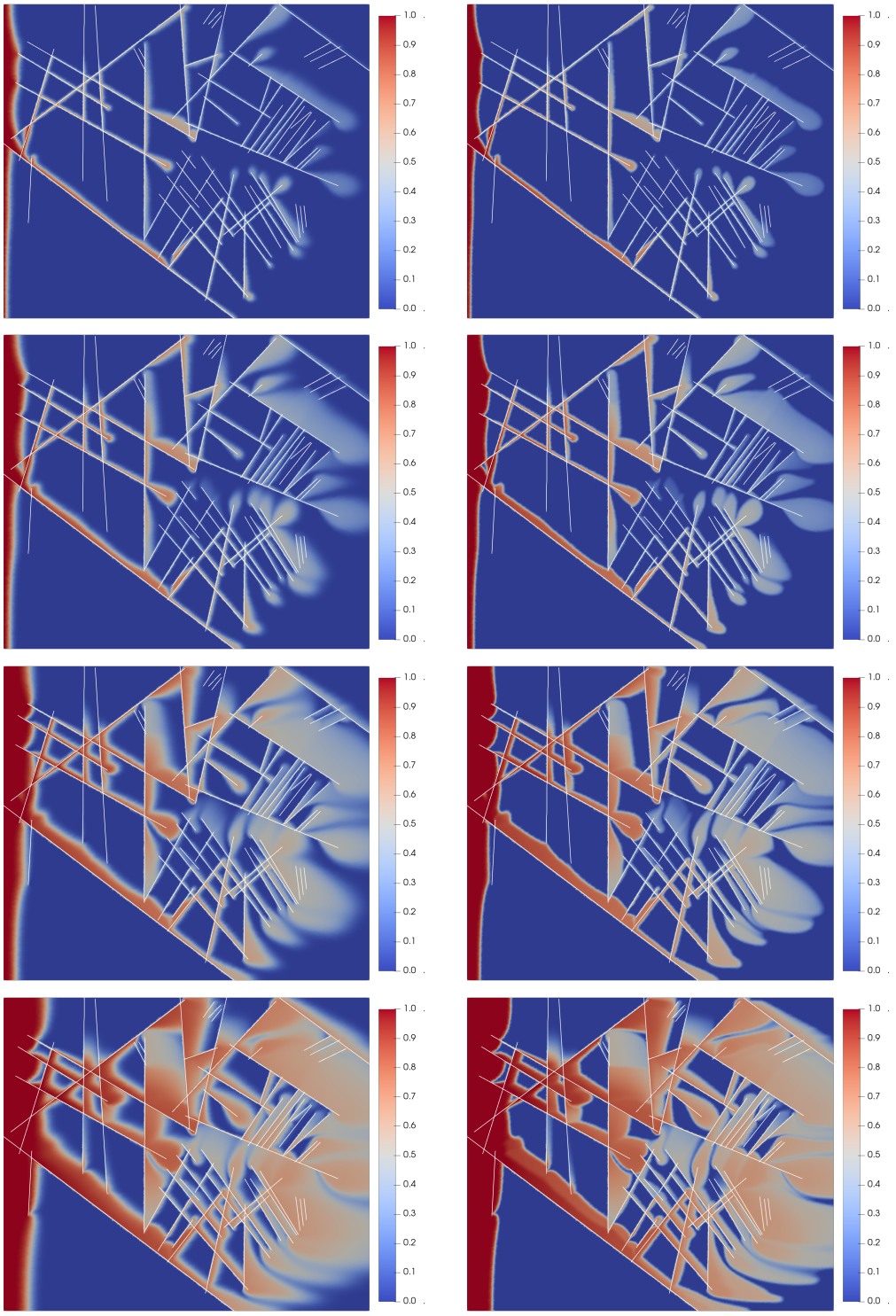

Figure 11: Approximate solution using the first-order implicit (left) and the mixed-order semi-implicit (right) schemes at $t = 10, 20, 40$ and 80 (from top to bottom).

Setting $\widetilde{K}_{exp} = \widetilde{K}_{m,exp}$ and $\widetilde{K}_{imp} = \widetilde{K}_{m,imp} + \widetilde{K}_f$ we consider the following semi-implicit discretization

$$M\frac{c^{n+1}-c^n}{\Delta t} = \left(\widetilde{K}_{exp} + \overline{D}_{exp}(c^n)\right)c^n + \left(\widetilde{K}_{imp} + D_{imp}\right)c^{n+1} - \left(S^+c^{n+1} + S^-c_D\right), \quad (43)$$

ξ	$\#\mathcal{T}_{imp}(\xi)$	Δt_{stab}	Speed-up
0	0	0.0008881	1
0.01	8	0.0057353	6.5
0.05	34	0.0201959	22.7
0.1	89	0.0307692	34.7
0.2	311	0.0676590	76.2
0.3	1210	0.0795862	89.6
0.5	10622	0.1187648	133.7

Table 3: Size of the implicit zone, stable time step and the computational speed-up for the scheme (43) as the function of ξ.

where, as before, the edge diffusion operators $\overline{D}_{exp}$ and D_{imp} are constructed based on $\widetilde{K}_{exp} - RS(\widetilde{K}_{exp})$ and $\widetilde{K}_{imp} - RS(\widetilde{K}_{imp})$ respectively. The stable time step is derived from the condition similar to (40) using $\widetilde{K}_{exp}$ instead of $\widetilde{K}_m$.

The table 3 reports the number of elements in $\mathcal{T}_{imp}(\xi)$ and the stable time step for the scheme (43) with the threshold parameter $\xi = 0.01, 0.05, 0.1, 0.2, 0.3, 0.5$. The value $\xi = 0$ leads to the reference semi-implicit scheme (38). The last column of Table 3 reflects the obtained computational speed-up defined as the ration of $N_T(0)$ over $N_T(\xi)$, where $N_T(\xi)$ denotes the total number of time steps as the function of ξ. We observe that by incorporating a very small portions of the matrix elements into the implicit zone the stable time step can be increased by almost two orders of magnitude. Taking a large enough ξ would eventually result in a fully implicit scheme, note however that increasing the size of $\mathcal{T}_{imp}$ above 311 elements ($\xi = 0.2$) does not lead to a considerable improvement in terms of the stable time step.

Figure 12 reports the location of the high CFL cells incorporated in $\mathcal{T}_{imp}(0.05)$ and $\mathcal{T}_{imp}(0.2)$. The highest CFL cells with $\xi_T \geq 0.05$ are essentially associated with fracture network discontinuities (see Figure 13). The regions with a slightly lower CFL are located at the fracture tips.

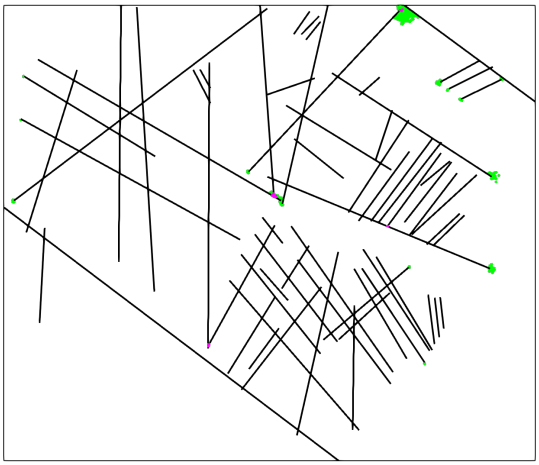

Figure 12: Implicit zones $\mathcal{T}_{imp}(0.05)$ (purple) and $\mathcal{T}_{imp}(0.2)$ (green).

As for the numerical error, we report on Figure 14 the weighted L^1 distance from the solution obtained by (43) to the reference solution provided by (38) as the function of time. Note that because the schemes (38) and (43) do not use the same time steps, the calculation of the L^1 distance involves the linear interpolations of the results provided by (43) between the time steps. For the sake of comparison Figure 14 equally reports the results obtained by the low-order scheme (39). We observe that the precision of the method is preserved for small values of ξ especially in the matrix domain. The higher values of the L^1 fracture distance at small times can be attributed to the fact that the scheme (43) uses larger time steps, and thus is less capable of capturing the fast transport in the fracture network and it vicinity.

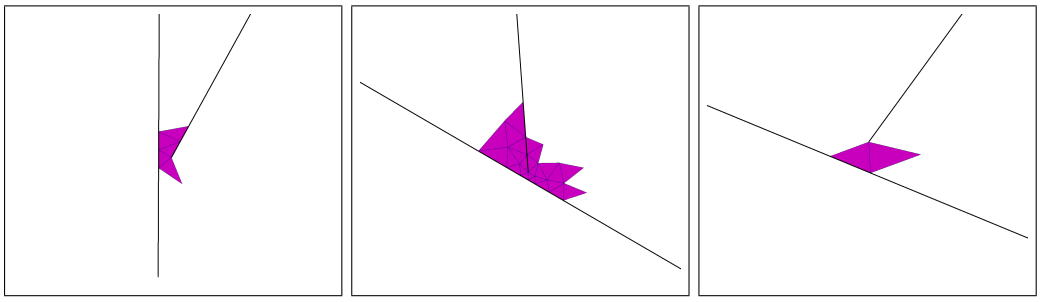

Figure 13: Zoom on the high CFL zone $\mathcal{T}_{imp}(0.05)$ around fracture network discontinuities.

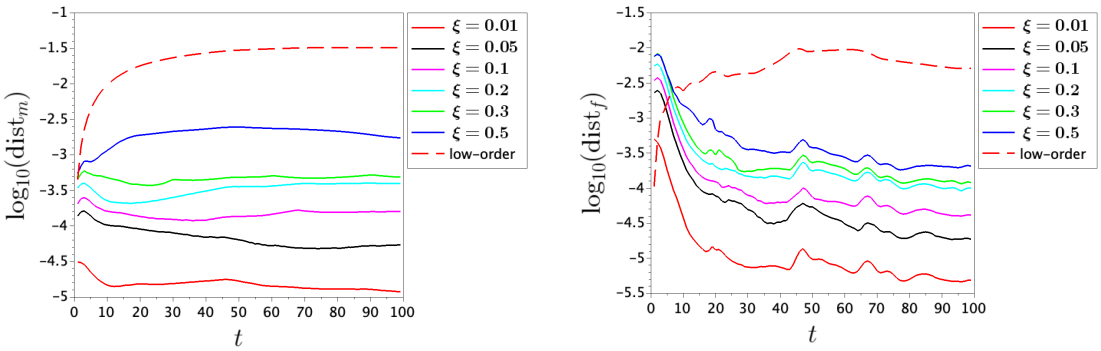

Figure 14: Weighed L_1 distance between the approximate solutions form the matrix (left) and the fracture network (right) domains.

5 Conclusion

We have introduced and studied a higher-order nodal numerical method for the hybrid-dimensional model of the solute transport in fractured porous media coupled to the Darcy flow problem. The numerical discretization of the transport problem combines the lumped piece-wise linear FE method with the Algebraic Flux Correction procedure leading to the family of nonlinear schemes that satisfy the local and the global versions of the Discrete Maximum Principle, while introducing a very limited amount of numerical diffusion. The numerical discretization that we have introduced can interpreted as a locally conservative nodal finite volume method. Another feature of the proposed method is that it's construction only relies on the standard FE stiffness and mass matrices, and the mesh topology. As the result this numerical method can be easily implemented in the existing FE codes, or extended to other discretization methods such as for example the Vertex Approximate Gradient scheme [10], [48]. In order to relax the global time constraint of the explicit time stepping schemes, we have proposed a mixed-order semi-implicit strategy, where the matrix domain is discretized using the higher-order nonlinear FE-AFC method, while the fracture domain is treated with the low-order implicit scheme.

We have performed the numerical convergence analysis for both fully explicit and semi-implicit approaches based on a simple test configuration, where the analytical solution is available. As expected, compared to the lower-order methods, the use of the FE-AFC discretization allows to reduce significantly the amount of numerical diffusion. For a low permeability contrast between fracture and matrix domains the comparison of the higher-order explicit scheme to the mixed-order semi-implicit approach shows that the latter one is sufficient to capture accurately the concentration profiles at the matrix transport time scale. In contrast to the fully explicit discretization, this semi-implicit method allows to address the flow scenario that exhibits the high permeability contrast between matrix and fracture domains.

We have further applied the semi-implicit FE-AFC method to the problem involving a complex fracture network. Here again, compared to the low-order upwind discretization the mixed-order FE-AFC method leads to a much sharper and detailed solution. Finally we have shown that the stable time step can be drastically increased by extending the implicit time stepping zone over a small portion of high CFL the matrix mesh elements associated with the discontinuities of the fracture network as well as some of the fracture tips.

Data Availability Statements

The datasets generated during and/or analysed during the current study are available from the corresponding author on reasonable request.

Conflict of Interest/Competing Interest Statement

The authors have no competing interests to declare that are relevant to the content of this article.

Acknowledgments

This project was funded by the National Plan for Science, Technology and Innovation (MAARIFAH), King Abdulaziz City for Science and Technology, Kingdom of Saudi Arabia, award number 14-MAT739-02.

References

[1] J. Aghili, K. Brenner, J. Hennicker, R. Masson, and L. Trenty. Two-phase discrete fracture matrix models with linear and nonlinear transmission conditions. *GEM-International Journal on Geomathematics*, 10(1):1–35, 2019.

[2] C. Alboin, J. Jaffré, J. E. Roberts, and C. Serres. Modeling fractures as interfaces for flow and transport. *Fluid Flow and Transport in Porous Media, Mathematical and Numerical Treatment*, 295:13, 2002.

[3] G. R. Barrenechea, V. John, and P. Knobloch. An algebraic flux correction scheme satisfying the discrete maximum principle and linearity preservation on general meshes. *Mathematical Models and Methods in Applied Sciences*, 27(03):525–548, 2017.

[4] G. R. Barrenechea, V. John, P. Knobloch, and R. Rankin. A unified analysis of algebraic flux correction schemes for convection–diffusion equations. *SeMA Journal*, 75(4):655–685, 2018.

[5] I. Berre, W. M. Boon, B. Flemisch, A. Fumagalli, D. Gläser, E. Keilegavlen, A. Scotti, I. Stefansson, A. Tatomir, K. Brenner, et al. Verification benchmarks for single-phase flow in three-dimensional fractured porous media. *Advances in Water Resources*, 147:103759, 2021.

[6] I. Berre, F. Doster, and E. Keilegavlen. Flow in fractured porous media: A review of conceptual models and discretization approaches. *Transport in Porous Media*, 130(1):215–236, 2019.

[7] K. Brenner, M. Groza, C. Guichard, and R. Masson. Vertex approximate gradient scheme for hybrid dimensional two-phase darcy flows in fractured porous media. *ESAIM: Mathematical Modelling and Numerical Analysis*, 49(2):303–330, 2015.

[8] K. Brenner, M. Groza, L. Jeannin, R. Masson, and J. Pellerin. Immiscible two-phase darcy flow model accounting for vanishing and discontinuous capillary pressures: application to the flow in fractured porous media. *Computational Geosciences*, 21(5):1075–1094, 2017.

[9] K. Brenner, J. Hennicker, and R. Masson. Nodal discretization of two-phase discrete fracture matrix models. *Polyhedral Methods in Geosciences*, pages 73–118, 2021.

[10] K. Brenner, J. Hennicker, R. Masson, and P. Samier. Hybrid-dimensional modelling of two-phase flow through fractured porous media with enhanced matrix fracture transmission conditions. *Journal of Computational Physics*, 357:100–124, 2018.

[11] F. Chave, D. A. Di Pietro, and L. Formaggia. A hybrid high-order method for passive transport in fractured porous media. *GEM-International Journal on Geomathematics*, 10(1):1–34, 2019.

[12] E. Flauraud, F. Nataf, I. Faille, and R. Masson. Domain decomposition for an asymptotic geological fault modeling. *Comptes Rendus Mécanique*, 331(12):849–855, 2003.

[13] B. Flemisch, I. Berre, W. Boon, A. Fumagalli, N. Schwenck, A. Scotti, I. Stefansson, and A. Tatomir. Benchmarks for single-phase flow in fractured porous media. *Advances in Water Resources*, 111:239–258, 2018.

[14] S. Geiger-Boschung, S. K. Matthäi, J. Niessner, and R. Helmig. Black-oil simulations for three-component, three-phase flow in fractured porous media. *SPE journal*, 14(02):338–354, 2009.

[15] H. Guo, W. Feng, Z. Xu, and Y. Yang. Conservative numerical methods for the reinterpreted discrete fracture model on non-conforming meshes and their applications in contaminant transportation in fractured porous media. *Advances in Water Resources*, 153:103951, 2021.

[16] H. Hoteit and A. Firoozabadi. Multicomponent fluid flow by discontinuous galerkin and mixed methods in unfractured and fractured media. *Water Resources Research*, 41(11), 2005.

[17] H. Hoteit and A. Firoozabadi. Compositional modeling of discrete-fractured media without transfer functions by the discontinuous galerkin and mixed methods. *SPE journal*, 11(03):341–352, 2006.

[18] H. Hoteit and A. Firoozabadi. An efficient numerical model for incompressible two-phase flow in fractured media. *Advances in Water Resources*, 31(6):891–905, 2008.

[19] H. Hoteit and A. Firoozabadi. Numerical modeling of two-phase flow in heterogeneous permeable media with different capillarity pressures. *Advances in water resources*, 31(1):56–73, 2008.

[20] A. Jha and V. John. A study of solvers for nonlinear afc discretizations of convection–diffusion equations. *Computers & Mathematics with Applications*, 78(9):3117–3138, 2019.

[21] A. Jha, O. Pártl, N. Ahmed, and D. Kuzmin. An assessment of solvers for algebraically stabilized discretizations of convection-diffusion-reaction equations. *arXiv preprint arXiv:2110.15676*, 2021.

[22] J. Jiang and R. M. Younis. An efficient fully-implicit multislope muscl method for multiphase flow with gravity in discrete fractured media. *Advances in Water Resources*, 104:210–222, 2017.

[23] J. Jiang and R. M. Younis. An improved projection-based embedded discrete fracture model (pedfm) for multiphase flow in fractured reservoirs. *Advances in water resources*, 109:267–289, 2017.

[24] D. Kuzmin. Positive finite element schemes based on the flux-corrected transport procedure. *Computational Fluid and Solid Mechanics, Elsevier*, pages 887–888, 2001.

[25] D. Kuzmin and M. Möller. Algebraic flux correction i. scalar conservation laws. In *Flux–Corrected Transport: Principles, Algorithms and Applications*. Springer, 2005.

[26] D. Kuzmin and M. Möller. Algebraic flux correction ii. compressible euler equations. In *Flux–Corrected Transport: Principles, Algorithms and Applications*, pages 207–250. Springer, 2005.

[27] D. Kuzmin, M. J. Shashkov, and D. Svyatskiy. A constrained finite element method satisfying the discrete maximum principle for anisotropic diffusion problems. *Journal of Computational Physics*, 228(9):3448–3463, 2009.

[28] D. Kuzmin and S. Turek. Flux correction tools for finite elements. *Journal of Computational Physics*, 175(2):525–558, 2002.

[29] C. Lohmann. On the solvability and iterative solution of algebraic flux correction problems for convection-reaction equations. 2019.

[30] C. Lohmann. Physics–compatible finite element methods for scalar and tensorial advection problems. 2019.

[31] C. Lohmann. An algebraic flux correction scheme facilitating the use of newton-like solution strategies. *Computers & Mathematics with Applications*, 84:56–76, 2021.

[32] V. Martin, J. Jaffré, and J. E. Roberts. Modeling fractures and barriers as interfaces for flow in porous media. *SIAM Journal on Scientific Computing*, 26(5):1667–1691, 2005.

[33] S. K. Matthäi, H. M. Nick, C. Pain, and I. Neuweiler. Simulation of solute transport through fractured rock: a higher-order accurate finite-element finite-volume method permitting large time steps. *Transport in porous media*, 83(2):289–318, 2010.

[34] J. Monteagudo and A. Firoozabadi. Control-volume method for numerical simulation of two-phase immiscible flow in two-and three-dimensional discrete-fractured media. *Water resources research*, 40(7), 2004.

[35] J. Monteagudo and A. Firoozabadi. Comparison of fully implicit and impes formulations for simulation of water injection in fractured and unfractured media. *International journal for numerical methods in engineering*, 69(4):698–728, 2007.

[36] J. E. Monteagudo and A. Firoozabadi. Control-volume model for simulation of water injection in fractured media: incorporating matrix heterogeneity and reservoir wettability effects. *SPE journal*, 12(03):355–366, 2007.

[37] M. G. C. Nestola and M. Favino. A novel equi-dimensional finite element method for flow and transport in fractured porous media satisfying discrete maximum principle and conservation properties. *arXiv preprint arXiv:2011.08804*, 2020.

[38] H. M. Nick and S. Matthäi. Comparison of three fe-fv numerical schemes for single- and two-phase flow simulation of fractured porous media. *Transport in porous media*, 90(2):421–444, 2011.

[39] V. Reichenberger, H. Jakobs, P. Bastian, and R. Helmig. A mixed-dimensional finite volume method for two-phase flow in fractured porous media. *Advances in water resources*, 29(7):1020–1036, 2006.

[40] W. C. Rheinboldt. *Methods for solving systems of nonlinear equations*. SIAM, 1998.

[41] P. Roe. *Numerical algorithms for the linear wave equation*. Royal Aircraft Establishment, 1981.

[42] K. S. Schmid, S. Geiger, and K. S. Sorbie. Higher order fe–fv method on unstructured grids for transport and two-phase flow with variable viscosity in heterogeneous porous media. *Journal of Computational Physics*, 241:416–444, 2013.

[43] J. R. Shewchuk. A two-dimensional quality mesh generator and delaunay triangulator. *Computer Science Division University of California at Berkeley, Berkeley, California, http://www. cs. cmu. edu/quake/triangle. html*, pages 94720–1776, 2008.

[44] P. K. Sweby. High resolution schemes using flux limiters for hyperbolic conservation laws. *SIAM journal on numerical analysis*, 21(5):995–1011, 1984.

[45] B. Van Leer. Towards the ultimate conservative difference scheme. ii. monotonicity and conservation combined in a second-order scheme. *Journal of computational physics*, 14(4):361–370, 1974.

[46] Y. Xie and M. G. Edwards. Higher resolution unstructured spectral finite-volume method for flow in porous media. In *SPE Reservoir Simulation Conference*. OnePetro, 2019.

[47] Y. Xie and M. G. Edwards. Higher resolution hybrid-upwind spectral finite-volume methods, for flow in porous and fractured media on unstructured grids. In *SPE Reservoir Simulation Conference*. OnePetro, 2021.

[48] F. Xing, R. Masson, and S. Lopez. Parallel vertex approximate gradient discretization of hybrid dimensional darcy flow and transport in discrete fracture networks. *Computational Geosciences*, 21(4):595–617, 2017.

[49] X. Zhang and C.-W. Shu. Maximum-principle-satisfying and positivity-preserving high-order schemes for conservation laws: survey and new developments. *Proceedings of the Royal Society A: Mathematical, Physical and Engineering Sciences*, 467(2134):2752–2776, 2011.

[50] A. Zidane and A. Firoozabadi. An efficient numerical model for multicomponent compressible flow in fractured porous media. *Advances in water resources*, 74:127–147, 2014.

Appendix A. Case 4.1: Approximate solution for $\Lambda_f = 20$

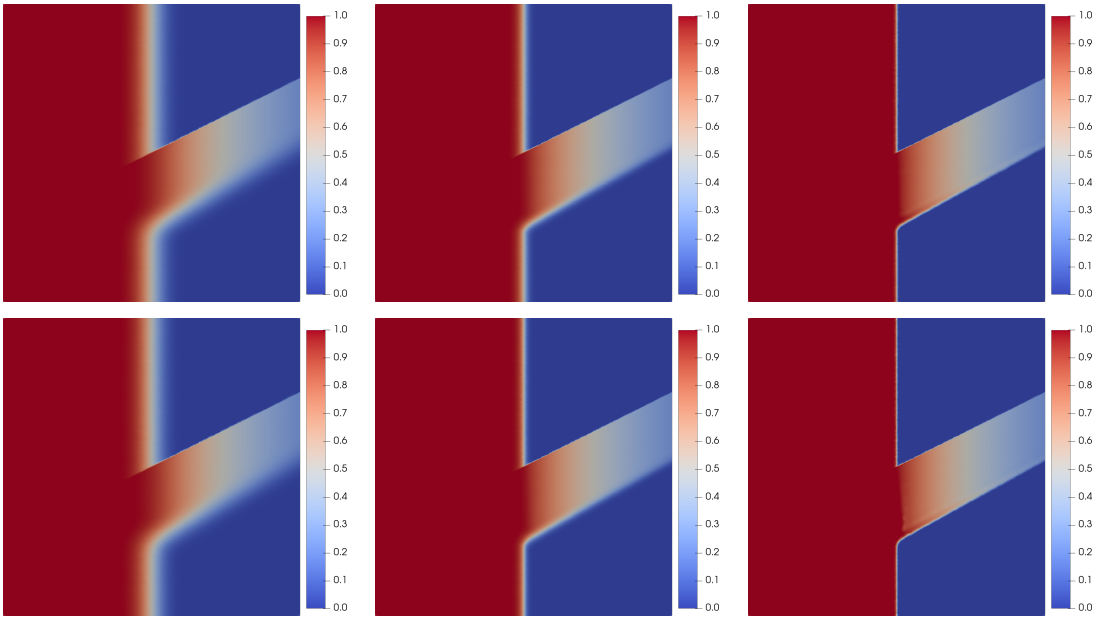

Figure 15: Approximate solution at $t = T_f$ using, left column: $o1$-explicit (top) and $o1$-semi-implicit (bottom) schemes; middle column: $o2$-explicit (top) and $o1$-$o2$-semi-implicit (bottom) schemes with **minmod** limiter; and right column: $o2$-explicit (top) and $o1$-$o2$-semi-implicit (bottom) schemes with **superbee** limiter.

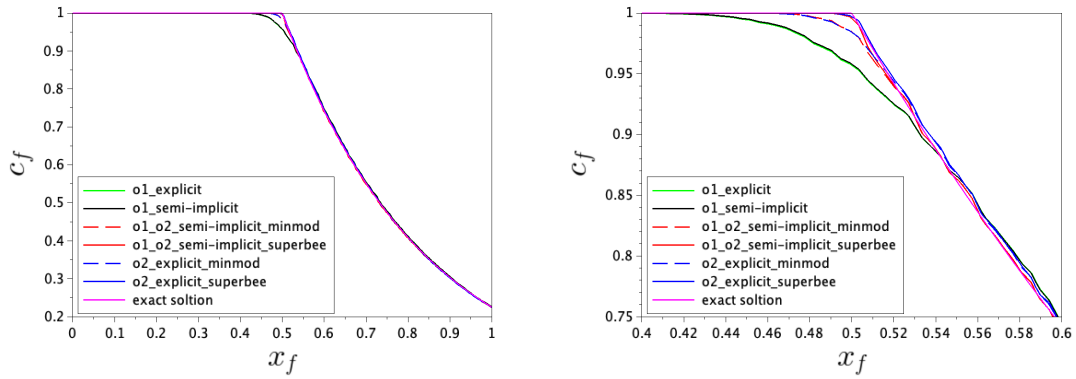

Figure 16: Left: approximate and exact solution along the fracture at $t = T_f$. Right: zoom view of left figure around $x = 0.5$. Fracture length is rescaled.

Appendix A. Case 4.1: Approximate solution for $\Lambda_f = 2000$

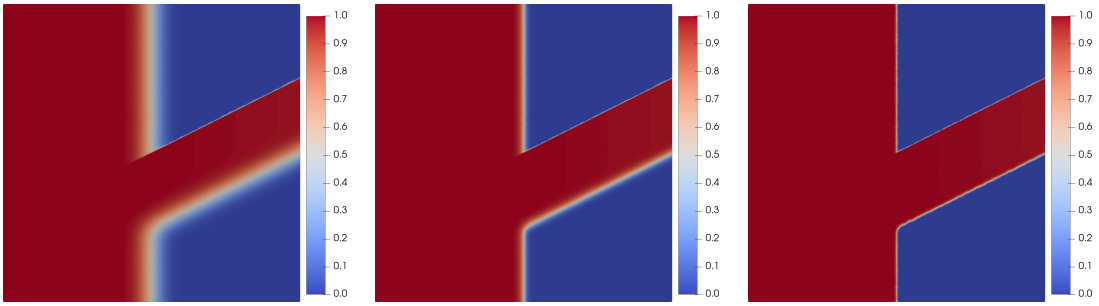

Figure 17: Approximate solution at $t = T_f$ using, left column: $o1$-explicit (top) and $o1$-semi-implicit (bottom) schemes; middle column: $o2$-explicit (top) and $o1$-$o2$-semi-implicit (bottom) schemes with **minmod** limiter; and right column: $o2$-explicit (top) and $o1$-$o2$-semi-implicit (bottom) schemes with **superbee** limiter.

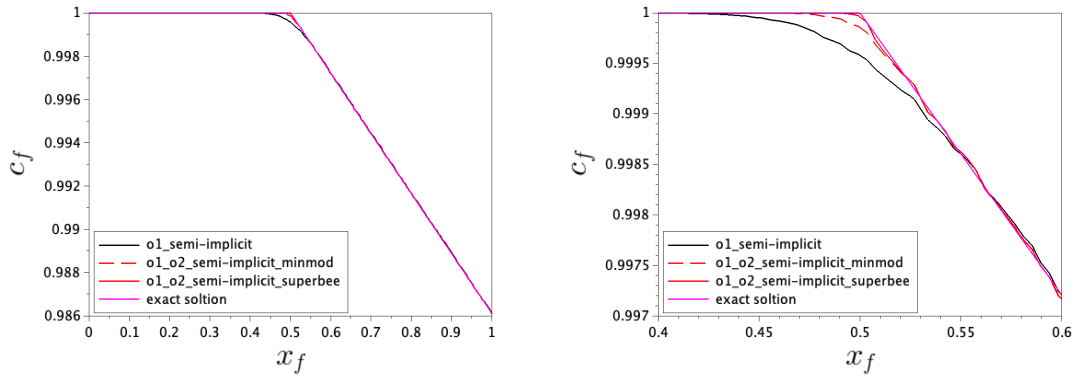

Figure 18: Left: approximate and exact solution along the fracture at $t = T_f$. Right: zoom view of left figure around $x = 0.5$. Fracture length is rescaled.

Appendix B. Case 4.1: L_1 relative space-time error

	$o1$-explicit				$o2$-exp. minmod				$o2$-exp. superbee			
Mesh	err_m	eoc	err_f	eoc	err_m	eoc	err_f	eoc	err_m	eoc	err_f	eoc
1	0.391	-	0.2043	-	0.3002	-	0.1971	-	0.2525	-	0.2177	-
2	0.2504	0.4023	0.106	0.5918	0.1579	0.5797	0.09682	0.6415	0.1082	0.7649	0.1068	0.6432
3	0.1457	0.4702	0.03405	0.987	0.07451	0.6525	0.02907	1.045	0.03839	0.9004	0.03369	1.002
4	0.08323	0.4865	0.01351	0.8031	0.03589	0.6344	0.01049	0.8855	0.01332	0.9193	0.01247	0.8633

Table 4: Relative L^1 space-time error and the experimental order of convergence for explicit schemes (case $\Lambda_f = 20$).

	$o1$-semi-implicit				$o1$-$o2$-semi-imp. minmod				$o1$-$o2$-semi-imp. superbee			
Mesh	err_m	eoc	err_f	eoc	err_m	eoc	err_f	eoc	err_m	eoc	err_f	eoc
1	0.3887	-	0.2043	-	0.295	-	0.1812	-	0.2391	-	0.1697	-
2	0.2449	0.4168	0.1046	0.6045	0.1505	0.6075	0.0883	0.6491	0.09781	0.8069	0.08027	0.6759
3	0.1417	0.4751	0.03332	0.9935	0.0692	0.6749	0.02843	0.9846	0.03345	0.9321	0.02668	0.957
4	0.08118	0.4841	0.01331	0.7972	0.03258	0.6543	0.01009	0.9	0.01147	0.9296	0.009605	0.8874

Table 5: Relative L^1 space-time error and the experimental order of convergence for semi-implicit schemes (case $\Lambda_f = 20$).

	$o1$-semi-implicit				$o1$-$o2$-semi-imp. minmod				$o1$-$o2$-semi-imp. superbee			
Mesh	err_m	eoc	err_f	eoc	err_m	eoc	err_f	eoc	err_m	eoc	err_f	eoc
1	0.3867	-	0.007856	-	0.3061	-	0.007748	-	0.2581	-	0.00771	-
2	0.2711	0.3206	0.00347	0.7375	0.1723	0.5186	0.003247	0.785	0.1165	0.7176	0.003151	0.8076
3	0.1602	0.4571	0.00143	0.7701	0.0819	0.6461	0.001368	0.7509	0.0414	0.899	0.001345	0.7396
4	0.09183	0.4831	0.000608	0.7429	0.03864	0.6526	0.000565	0.7681	0.01408	0.9367	0.000555	0.7689

Table 6: Relative L^1 space-time error and the experimental order of convergence for semi-implicit schemes (case $\Lambda_f = 2000$).